JOURNAL OF GEOPHYSICAL RESEARCH, VOL. 113, B10317, doi:10.1029/2007JB005184, 2008

A model of earthquake triggering probabilities and application to dynamic deformations constrained by ground motion observations

Joan Gomberg[1] and Karen Felzer[2]

Received 25 May 2007; revised 3 July 2008; accepted 4 August 2008; published 31 October 2008.

[1] We have used observations from Felzer and Brodsky (2006) of the variation of linear aftershock densities (i.e., aftershocks per unit length) with the magnitude of and distance from the main shock fault to derive constraints on how the probability of a main shock triggering a single aftershock at a point, $P(r, D)$, varies as a function of distance, r, and main shock rupture dimension, D. We find that $P(r, D)$ becomes independent of D as the triggering fault is approached. When $r \gg D$ $P(r, D)$ scales as D^m where $m \sim 2$ and decays with distance approximately as r^{-n} with $n = 2$, with a possible change to $r^{-(n-1)}$ at $r > h$, where h is the closest distance between the fault and the boundaries of the seismogenic zone. These constraints may be used to test hypotheses about the types of deformations and mechanisms that trigger aftershocks. We illustrate this using dynamic deformations (i.e., radiated seismic waves) and a posited proportionality with $P(r, D)$. Deformation characteristics examined include peak displacements, peak accelerations and velocities (proportional to strain rates and strains, respectively), and two measures that account for cumulative deformations. Our model indicates that either peak strains alone or strain rates averaged over the duration of rupture may be responsible for aftershock triggering.

Citation: Gomberg, J., and K. Felzer (2008), A model of earthquake triggering probabilities and application to dynamic deformations constrained by ground motion observations, *J. Geophys. Res.*, *113*, B10317, doi:10.1029/2007JB005184.

1. Introduction

[2] The desire to produce time-dependent earthquake forecasts that account for how deformations arising from one earthquake affect the likelihood of occurrence of another motivates many earthquake triggering studies. More generally, we would like to understand what causes earthquake ruptures to nucleate. Observations of the temporal behavior of aftershocks have provided important constraints on the nucleation process and viable physical models [*Dieterich*, 1994; *Gomberg*, 2001; *Freed*, 2005; *Steacy et al.*, 2005]. We look to the spatial behavior of aftershocks to provide new constraints on how the probability of triggering an aftershock at a point must scale with the size of and distance from the triggering earthquake. As an example of how this information might be used, we test the hypothesis that the probability of triggering is proportional to posited characteristics of dynamic deformations (i.e., those associated with transient, oscillatory, seismic waves).

[3] The development of our probability model begins with observations of linear aftershock densities, or aftershocks per unit length, $\rho(r)$, documented by *Felzer and Brodsky* [2006]. Particularly noteworthy features of the aftershock densities measured by *Felzer and Brodsky* [2006] are the constancy of the decay rate with distance, regardless of the main shock rupture dimension. We describe aftershock densities as the joint probability of the likelihood of encountering a nucleation site (i.e., a fault or fault segment) at distance, r, from a main shock of rupture dimension, D, or $N(r, D)$, and the likelihood of failure being triggered at that nucleation site by deformations associated with that main shock, $P(r, D)$. Herein r refers to the closest distance between the aftershock hypocenter and the main shock rupture plane. This description may be written mathematically as

$$\rho(r) = \frac{N(r, D)}{\Delta r} P(r, D) \tag{1}$$

Since the aftershock density given by *Felzer and Brodsky* [2006] is a linear measure, $N(r, D)$ describes the total number of nucleation sites that exist within a unit distance, Δr, from r (i.e., between $r \pm \Delta r/2$) (see Table 1 for a listing of notation).

[4] A primary goal of this study is to derive a model of the second component of this joint probability of equation (1), $P(r, D)$, the probability that an aftershock will be triggered at a given available nucleation site. On the basis of equation (1), we derive a model of $P(r, D)$ using observations of linear aftershock densities, $\rho(r)$, and employing a statistical model of the distribution of potential nucleation sites, $N(r, D)$. Since for triggered aftershocks $N(r, D)$ is not known a priori, it is necessary to construct a

[1] U. S. Geological Survey, Department of Earth and Space Sciences, University of Washington, Seattle, Washington, USA.
[2] U. S. Geological Survey, Pasadena, California, USA.

Table 1. Notation

Variable	Value
	Physical Parameters
r	closest distance between triggering and potentially triggered sites
M	magnitude of the triggering earthquake
$M_{\min}$	minimum magnitude of completion of the catalog used
D	main shock rupture dimension
V	volume of a shell surrounding the main shock fault. everywhere at distance r from it with width Δr
h	distance to the top or bottom the seismogenic layer
H	seismogenic layer thickness
V_r	rupture velocity
	Empirical or Measured Parameters
γ	constant describing power law distance-decay rate of linear aftershock densities
C	constant of proportionality between linear aftershock densities and $10^{M-M\min}r^{-\gamma}$
d	effective dimensionality of the system of faults or nucleation sites
A	aggregate density of nucleation sites within the crust in a region
$pK(r, D)$	peak value of seismic waves observed at r from a rupture of dimension D
T	duration of seismic waves observed at r from a rupture of dimension D
K	proportionality constant between seismic deformation and probability
	Functions
$\rho(r)$	linear aftershock or earthquake density
$N(r, D)$	total number of potential nucleation sites
$F(r)$	number of nucleation sites per unit volume
$P(r, D)$	probability that a deformation associated with a main shock of rupture dimension D at distance r will trigger failure
$g(r, D, t)$	time-varying displacement, velocity or accelerations associated with passing seismic waves observed at r from a rupture of dimension D
$\xi(D)$	functional form in attenuation relation of *Campbell and Bozorgnia* [2007]

model, so that the estimate of $P(r, D)$ here is strictly an inference. We emphasize two points here, the first being that our objective is to capture only the first-order features of the scaling of $P(r, D)$ with r and D. This is appropriate because the aftershock densities that constrain $P(r, D)$ represent stacks from many main shocks, our model of $N(r, D)$ is statistical in nature, and the hypotheses we test using $P(r, D)$ include measurements from many earthquakes. The second point is that the derivation of $P(r, D)$ does not involve any a priori assumptions about its dependence on r and D and moreover, that it is completely independent of whatever the posited causative deformations might be or their relationship (linear or nonlinear) to $P(r, D)$ (see section 5.1).

[5] In the sections that follow we first describe the basic observations of $\rho(r)$ (section 2); next we present our statistical model of nucleation sites, $N(r, D)$ (section 3), and then infer and discuss what these imply about how triggering probabilities scale with distance from and the rupture dimension of causative main shocks (section 4). We conclude by illustrating how this scaling information may be used to test hypotheses about the viability of posited triggering deformations and their relationship to triggering probability, using dynamic deformation characteristics presumed proportional to triggering probability as an example (section 5).

2. Linear Aftershock Densities

[6] In this section we describe linear aftershock densities, $\rho(r)$, as they guide the development of our probability models. The measurement methodology and robustness are described by *Felzer and Brodsky* [2006] and its supplementary material so here we just summarize the salient features of the measured aftershock densities. *Felzer and Brodsky* [2006] made measurements of $\rho(r)$ and modeled them empirically with the relation

$$\rho(r) = C10^{M-M\min}r^{-\gamma} \tag{2a}$$

where M is the magnitude of the triggering earthquake, $M_{\min}$ is the minimum magnitude of the aftershocks measured, r is distance, and γ and C are constants. We show an example of $\rho(r)$ for data from *Felzer and Brodsky* [2006] in Figure 1. Note that on this graph only aftershocks of M 5–6 main shocks are plotted at distances <3 km and only aftershocks of M 2–3 main shocks are plotted at distances >3 km. Three kilometers is about 1 fault length of a M 5 earthquake and over 10 fault lengths of an M 3 earthquake [*Wells and Coppersmith*, 1994]. Thus, plotting the data in this manner clearly demonstrates that $\rho(r)$ is a constant over distances spanning a fraction of a main shock fault length to hundreds of main shock fault lengths, at least out to absolute distances of 50–100 km. The full distance range of aftershocks for M 2–6 main shocks is shown in the figures of *Felzer and Brodsky* [2006].

[7] While the main data set of *Felzer and Brodsky* [2006] was from Southern California, *Felzer and Brodsky* [2006] also measured aftershock distances in Northern California and Japan. In all locations they found an inverse power law decay of aftershock density with distance, with some variation in the power law exponent; while −1.37 was the exponent found in Southern California, −1.45 was found in Japan and −1.8 in Northern California.

[8] Prior to the publication of *Felzer and Brodsky* [2006], it was generally held that small main shocks did not trigger other earthquakes beyond distances of one two to fault lengths. That the earthquakes identified by *Felzer and Brodsky* [2006] are in fact distantly triggered aftershocks of small main shocks can be readily verified, however, by several different observations. First, the distantly triggered events adhere to the same steep inverse power law decay of density with distance as is seen for the near field aftershocks (Figure 1). This decay is in strong contrast to the more constant or increasing linear density with distance that characterizes normal background seismicity [*Kagan and Knopoff*, 1980; *Helmstetter et al.*, 2005; *Kagan*, 2007]. Second, the temporal decay rate of the distantly triggered earthquakes decays according to the modified Omori law [*Felzer*, 2005], which is highly characteristic of aftershock activity. Third, smaller earthquakes immediately preceding the target main shocks display the same inverse power law decay of density with distance from the main shocks as the purported triggered events (D. Marsan, personal communication, 2008). This is expected since foreshocks are just small main shocks with larger aftershocks [*Reasenberg and*

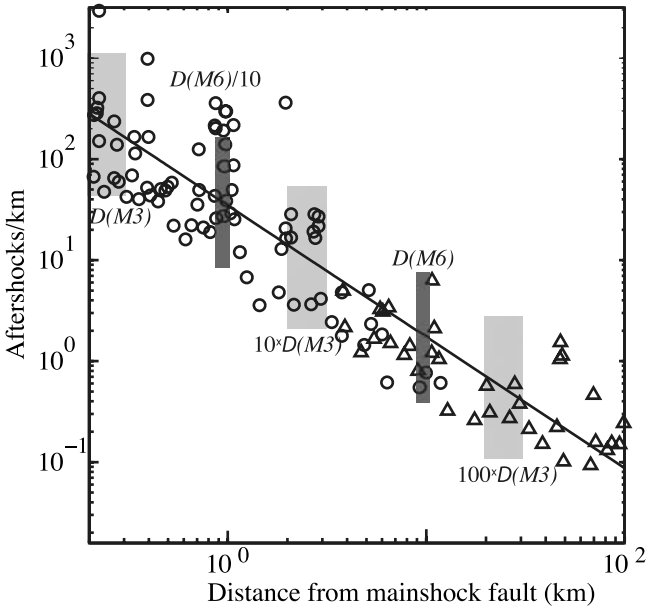

Figure 1. Measured linear aftershock densities. Catalog data are from the relocated 1984–2002 Southern California catalog of *Shearer et al.* [2005], with a subset of linear aftershocks density measurements from the study of *Felzer and Brodsky* [2006]. Main shocks are defined as earthquakes that are separated from larger main shocks by at least 100 km and by 3 days if the larger earthquake comes first, 0.5 days if it comes after. These separations ensure that we are looking at aftershocks of the intended main shock rather than at aftershocks of some larger earthquake. All aftershocks are M > 2 and occur in the first 5 min after their main shock; the short time window separates aftershocks from unrelated background earthquakes [*Bak et al.*, 2002]. Triangles and circles are for M2–3 and M5–6 main shocks, respectively. Note that we plot only a subset of aftershocks in each magnitude range, retaining only aftershocks of *M*5–6 main shocks at $r < 3$ km and of *M*2–3 main shocks at larger distances. This highlights the continuity in densities across the transition from near-field to far-field, which occurs at about $r \approx D \approx 3$ km for the M5–6 main shocks. The straight line is fit to the M2–3 data with an inverse power law with an exponent of 1.30 ± 0.1. Vertical shaded bands show the distances equal to one tenth to one hundred times the approximate rupture dimensions, D, of M3 and 6 earthquakes, estimated using the relations of *Wells and Coppersmith* [1994].

Jones, 1989; *Felzer et al.*, 2004] and so the distribution of distances between foreshocks and main shocks should be the same as the distributions between main shocks and aftershocks when the aftershocks are smaller.

[9] We rewrite the function for $\rho(r)$ found by *Felzer and Brodsky* [2006] in terms of the main shock rupture dimension, *D,* by substituting $D^2 \propto 10^M$ [*Hanks and Kanamori*, 1979; *Felzer et al.*, 2004; *Helmstetter et al.*, 2005, 2006], resulting in

$$\rho(r) = C10^{-M\,\min} D^2 r^{-\gamma} \tag{2b}$$

Figure 2 shows schematically that $\rho(r)$ measures the number of aftershocks within a volume shell, *V,* defined by a surface, *S*, that is everywhere at a distance *r* from the main shock rupture plane (not epicentral distance), and width Δr. (*Felzer and Brodsky* [2006] actually use the nearest neighbor method to determine aftershock density, but it is equivalent to the volume count and more robust.) We employ this same representation in the development of a model of the linear density of nucleation sites, *N(r, D)* Figure 3.

3. A Statistical Model of the Linear Density of Nucleation Sites, *N(r, D)*

[10] To derive a model of *N(r, D)*, the number of potential aftershock nucleation sites as a function of distance from the main shock fault plane, we use the same conceptual geometry that was used to measure the linear aftershock densities (Figure 2). Thus *N(r, D)* is the summation (integration) of all potential nucleation sites within a volume shell of width Δr that is everywhere a distance *r* from the main shock fault plane. The fact that $\rho(r)$ is derived from stacking measurements from many earthquakes implies that the distribution of nucleation sites cannot depend on absolute location, and as noted above, *r* does not represent an absolute location but rather the closest distance between the rupturing main shock fault plane and the potential aftershock hypocenter. Since we seek to capture only the statistical properties of *N(r, D)*, we assume there is a function *F(r)* that represents the number of nucleation sites per unit volume, which matches the true distribution in its statistical characteristics. Thus, *N(r, D)* may be derived by integrating *F(r)* over the volume shell that surrounds the main shock fault, is everywhere at distance *r*, and has width Δr, or

$$N(r,D) = \int_{V(r,D)} F(r)dv \approx F(r)S(r,D)\Delta r \tag{3}$$

As the references and discussion in the next paragraph indicate, there is precedent for the description of *F(r)* as

$$F(r) = Ar^{[d(r)-3]} \tag{4}$$

where *A* represents an average property of the crust in the region and *d* the dimensionality of the system. For reasons discussed below *d* may depend on *r* (*e.g.*, change beyond some distance related to the width of the seismogenic zone).

[11] Previous studies that measured the density of interevent distances from earthquake catalogs suggest that a purely statistical representation is sensible, and that a single power law function like equation (4) is appropriate [*Kagan and Knopoff*, 1980; *Helmstetter et al.*, 2005, *Kagan*, 2007]. They also show the distribution of nucleation sites cannot depend on absolute location, such that the distance *r* in *F(r)* may be locally defined, representing the distance between the triggering source and nucleation sites. In other words, they showed that the density does not depend on the location, magnitude, or the dimensions of the region considered and thus, must be a property of the crust that is scale-invariant and therefore can be locally defined. The results of *Felzer and Brodsky* [2006] corroborate this; if this were not true their stacking of measurements from earth-

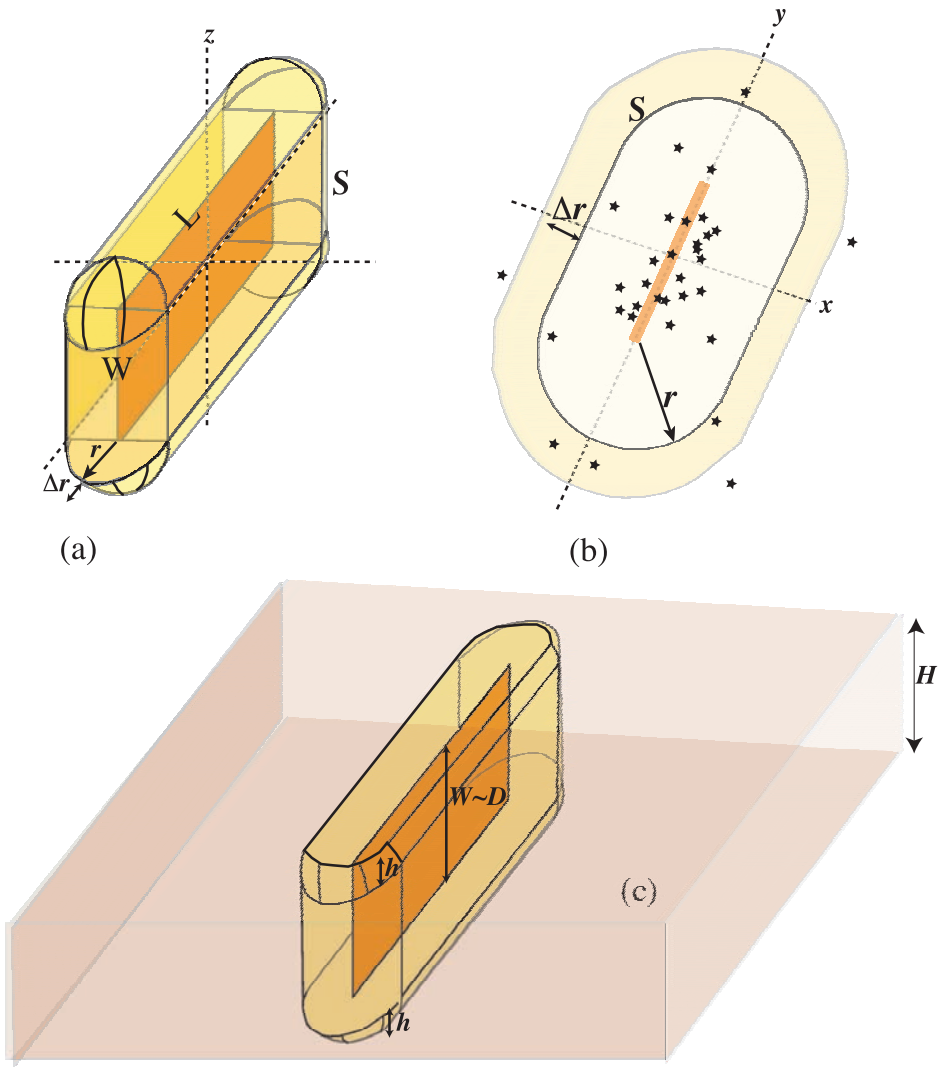

Figure 2. Cartoon of conceptual model employed in measuring and modeling linear aftershock densities, which effectively is a count of the number of aftershocks within a volume, *V*, surrounding the main shock rupture plane. (a) V is defined by a surface, *S*, that is everywhere a distance *r* from the rupture plane of length *L* and width *W*, and has width Δr. (b) When viewed in map view the aftershocks (stars) counted in the density at *r* are those within the shaded annulus. (c) For a vertical fault centered in a seismogenic layer of thickness *H*, when *r* equals $h = (H-D)/2$, the volume becomes truncated as shown. See text for more explanation.

quakes sampling different parts of the crust would not yield sensible results. *Kagan and Knopoff* [1980] and *Kagan* [1991] found that $d\sim2$ to 2.2 (for shallow earthquakes) for small to major earthquake magnitudes and very local to global distances. This implies a distribution of faults or nucleation sites that is statistically indistinguishable from a uniform distribution over an infinite plane (described as having fractal dimension 2), but also that may be consistent with a multitude of different complex fault systems. *Helmstetter et al.* [2005] estimated $d\sim2.1$ for magnitude 2 to 7.5 southern California earthquakes.

[12] One additional complication that must be considered is the change in the shape of the volume integrated over when the boundaries of the seismogenic zone are encountered. Let $r\sim h$ be the distance at which the boundaries of the seismogenic zone are reached. At $r\sim h$ the volume shell integrated over begins to change from one that grows with *r* in three dimensions to one that grows in two dimensions, and thus we expect the decay rate of $\rho(r)$ to decrease by a factor of *r* at about $r\sim h$. Notably, no such scale change in $\rho(r)$ (the rate of aftershock decay with distance) is observed.

[13] We consider two alternative, end-member interpretations of the lack of scale change in $\rho(r)$ with *h*, which lead to different inferences about the decay rate of $P(r, D)$. The first assumes that $\rho(r)$ is constant with distance because both $N(r, D)$ and $P(r, D)$ are constant with distance. Consistency of $N(r, D)$, or the total number of nucleation sites in a volume annuli at a given distance, in turn requires that $F(r)$, or the density of nucleation sites per unit volume, must change around $r\sim h$ (or at least $F(r)$ must change if we only count volume that is within the seismogenic zone; if we include nonseismogenic volume the average value of $F(r)$

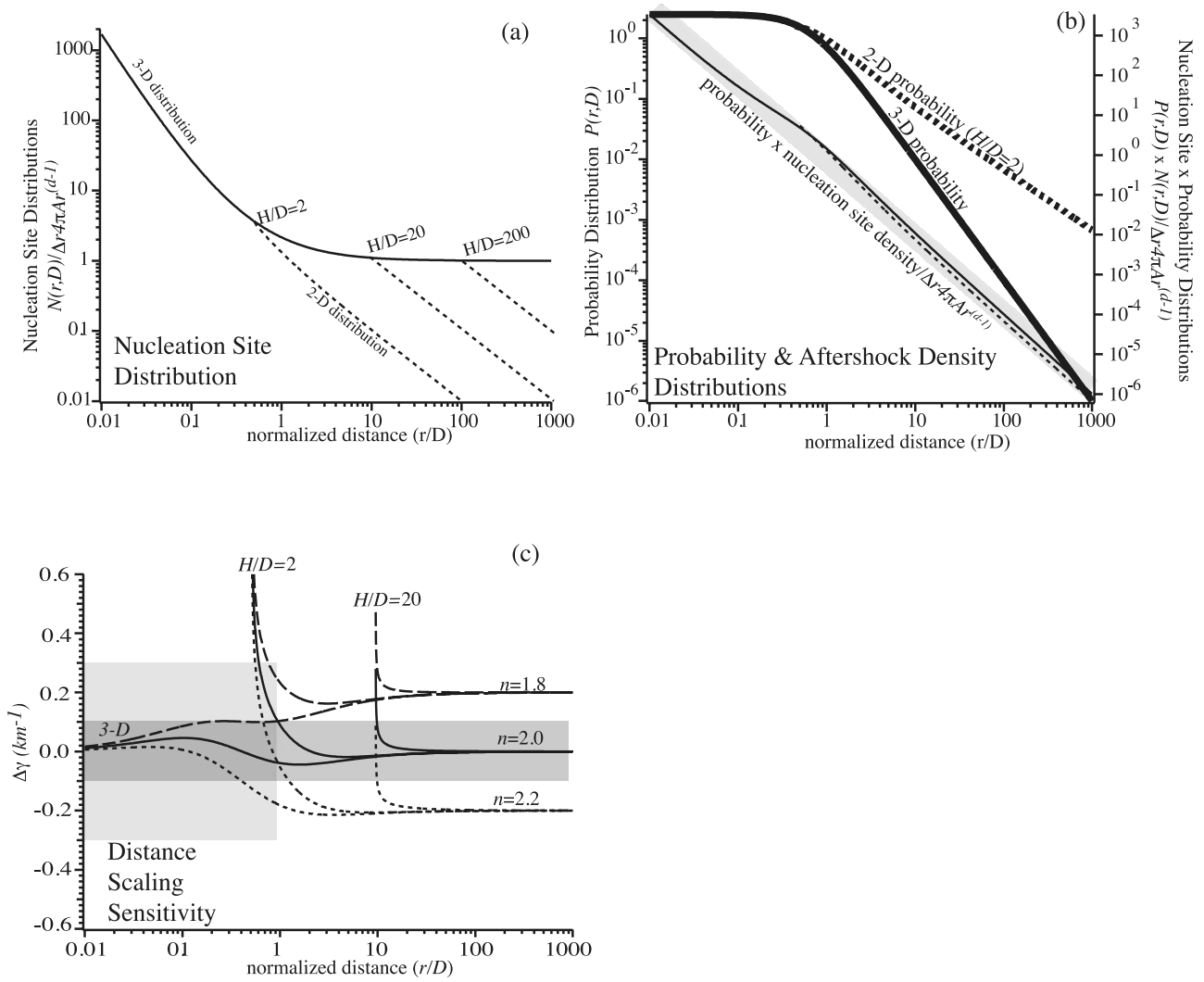

Figure 3. (a) Normalized integrated distribution of nucleation sites, *N(r, D)*, described by equations (5) normalized by the term $4\pi Ar^{(d-1)}$ so the curves do not depend on region-dependent factors A and d. r is normalized by D. The solid curve represents *N(r, D)* for the h-independent *P(r, D)* model at all distances or the h-dependent model at $r \leq h$ and the dashed curve to the h-dependent model at $r > h$ (see text). Examples for three values of *D/H* are shown (H is the width of the seismogenic layer) with estimates of values that would correspond approximately to H = 20 km and ruptures dimensions for M2, M 4, and M 6 earthquakes. (b) Probability distributions, *P(r, D)*, described by equation (8) (thick curves) for the h-independent *P(r, D)* case (solid) and an h-dependent *P(r, D)* case with *H/D* = 2 (dashed). When multiplied with the corresponding nucleation site distributions in Figure 3a, these should produce aftershock densities that have approximately constant power law decay rates; nucleation site distributions are normalized as in Figure 3a. (c) Estimates of the variation in γ, or $\Delta\gamma(r)$, for different values of n (labeled), calculated for h-dependent *P(r, D)* models in which $D = H/2$ and $D = H/20$ and for the h-independent *P(r, D)* model, which is independent of D when the normalized distance *r/D* is used. Shaded areas indicate $\Delta\gamma$ values estimated for measured aftershock densities in the work of *Felzer and Brodsky* [2006].

over the whole volume will remain constant). The second model assumes a lack of scale change in $\rho(r)$ with h because *N(r, D)* and *P(r, D)* both have scale changes at $r \sim h$ that compensate for one another. In this model *F(r)*, as expressed per unit of seismogenic volume, does not change at $r \sim h$. (We do not expect sharp scale changes even for earthquakes of the same size, because their varying depths imply a distribution of values of h.) Greater precedent exists for the second interpretation in published studies, as noted above in our discussion of *F(r)* (equation (4)). However, we cannot rule out the first alternative, noting that the aforementioned studies only infer properties of *F(r)* from linear (integrated) density measures of interevent spacing, and that *F(r)* is a statistical description of an undoubtedly complex distribution of a planar and clustered system of points or patches.

[14] With this in mind we can now evaluate the integral, equation (3), for the model in which *P(r, D)* and *N(r, D)* both depend on h. If we consider planar, rectangular faults

of length, L, and width, W, to adequately represent the average shape of all main shocks, the shell described by $S(r, D)$ is easily described and the integration easy to perform. We have not found other shapes that permit analytic expressions to be derived, but we suggest that whether analytic or numerical, the results would not be significantly different. For a rectangular fault S is comprised of (1) four quarter spheres of radius r each centered on a corner of the fault, (2) two half cylinders of radius r with axes of length L along the top and bottom edges of the fault, (3) two half cylinders of radius r with axes of length W along the sides of the fault, and (4) two planes of area LxW parallel to the fault at distances $\pm r$. The vector along r is everywhere perpendicular to S so that Δr is properly defined. The integral of equation (3) is

$$\begin{aligned}\frac{N(r,D)}{\Delta r} &= r^{d-3}A\left[4\pi r^2 + (2\pi rL + 2\pi rW) + 2WL\right] \\ &= r^{d-1}4\pi A\left[1 + \frac{D}{r} + \frac{1}{2\pi}\frac{D^2}{r^2}\right] \quad r \le \mathrm{h} \\ \frac{N(r,D)}{\Delta r} &= r^{d-1}4\pi A\left[1 - \left(1 - \frac{h}{r}\right)\right. \\ &\quad \left. + \frac{D}{r}\left\{1 - \frac{1}{\pi}\cos^{-1}\left(\frac{h}{r}\right)\right\} + \frac{1}{2\pi}\frac{D^2}{r^2}\right] r > \mathrm{h} \end{aligned} \tag{5}$$

For simplicity we have assumed a vertical, square fault centered within the seismogenic layer in which $L \sim W \sim D$. With these assumptions h depends on D, such that it equals half the difference between D and the width of the seismogenic layer. In reality h will depend on the focal depth and fault dip and the resulting model would be more complex than that represented by equation (5). The result for the model in which $P(r, D)$ and $N(r, D)$ remain constant when r reaches the boundaries of the seismogenic zone has the same form as equation (5) for $r \le h$, but this form also applies to all distances (i.e., $r > h$).

4. Inferences About the Probability of Triggering, $P(r, D)$

[15] Now that we have a statistical model of $N(r, D)/\Delta r$ (equation (5)) we can make inferences about $P(r, D)$ using the description of $\rho(r)$ embodied in equation (1). This description tells us that unknown $P(r, D)$ multiplied by the model of $N(r, D)/\Delta r$ (equation (5)) must equal the empirical description of $\rho(r)$ (equation (2)). This yields the equations

$$\begin{aligned} C10^{-M_{\min}}D^2r^{-\gamma} &= 4\pi A\left[1 + \frac{D}{r} + \frac{1}{2\pi}\frac{D^2}{r^2}\right]r^{d(r)-1}P(r,D) \quad r \le h \\ &= 4\pi A\left[1 - \left(1 - \frac{h}{r}\right) + \frac{D}{r}\left\{1 - \frac{1}{\pi}\cos^{-1}\left(\frac{h}{r}\right)\right\}\right. \\ &\quad \left. + \frac{1}{2\pi}\frac{D^2}{r^2}\right]r^{d-1}P(r,D) \quad r > h \\ &= 4\pi A\left[\frac{h}{r} + \frac{D}{r}\left\{1 - \frac{1}{\pi}\cos^{-1}\left(\frac{h}{r}\right)\right\}\right. \\ &\quad \left. + \frac{1}{2\pi}\frac{D^2}{r^2}\right]r^{d-1}P(r,D) \quad r > h \end{aligned} \tag{6}$$

The scale change at $r \sim h$ corresponds to the model in which $P(r, D)$ changes at h. If it does not change at h as described above, the above equality for $r \le h$ is true for all distances. These equalities require that in the near-field, when $r \ll D$,

$$P(r,D) \propto r^{-(d-3)-\gamma} r \ll D \tag{7a}$$

In the far-field, when $r \gg D$, for the model in which $P(r, D)$ changes at h, the equalities require that

$$\begin{aligned} P(r,D) &\propto D^2 r^{-(d-1)-\gamma} \quad r \le h \\ &\propto D^2 r^{-(d-2)-\gamma} \quad \mathrm{r} > \mathrm{h} \end{aligned} \tag{7b}$$

Simple power law functions that satisfy all these requirements are

$$\begin{aligned} &\frac{D^m}{(\alpha D + r)^n} \text{ or } \frac{D^m}{(\alpha D^n + r^n)} \quad r \le h \\ &\frac{D^m}{(\alpha D + r)^n}\frac{\left(\frac{r}{D} + 1\right)}{\left(\frac{h}{D} + 1\right)} \text{ or } \frac{D^m}{(\alpha D^n + r^n)}\frac{\left(\frac{r}{D} + 1\right)}{\left(\frac{h}{D} + 1\right)} \quad r > h \end{aligned} \tag{8}$$

If $P(r, D)$ does not change at h, then d effectively becomes $d(r, h)$ and the expressions at $r < h$ apply beyond h as well. Finally, the near-field equation (7a) requires that

$$\gamma = 3 - d \tag{9}$$

α is an empirical constant. *Felzer and Brodsky* [2006] find $\gamma \sim 1.4$ for Southern California corresponding to a constant value of $d \sim 1.6$. Note that the values of these two parameters may be different in other regions.

[16] To make expressions (8) consistent with equation (7b), we see that $m \sim 2$. An uncertainty of about ± 0.2 from the value of 2 is permissible based on the aftershock scaling data currently available in California (see Appendix A). Consistency and equality (9) further imply that $n = 2$. Therefore we are searching for a triggering deformation that satisfies $m = n = 2$.

5. Testing Posited Deformations and Their Probability of Triggering

[17] We now illustrate how this model of the scaling of triggering probabilities with the distance from and rupture dimension of triggering main shocks may be used to test hypotheses about posited triggering deformations and their relationship with triggering probability. We will show that some dynamic deformations are consistent with our expressions describing aftershock triggering probabilities if the relationship between the posited deformation and the triggering probability is linear, which is the most simple physical model. As already noted, the development of $P(r, D)$ (equation (8)) depends only on the empirical description of the aftershock densities and statistical model of the distribution of nucleation sites, and thus is completely independent of the causative deformation and physics relating it to nucleation or triggering. We hypothesize herein that specific measures of dynamic deformations may be linearly

related to *P(r, D)* (see section 5.1 for justification), but emphasize that other deformations and relationships may be proposed. For example, N. J. Van der Elst and E. E. Brodsky (Long and short range earthquake triggering as a function of seismic wave amplitude, submitted to *Nature*, 2008) suggest that triggering probability scales as the square root of peak velocity and *Dieterich* [1994] proposed a nonlinear relationship between static stress changes and triggering probability, with the latter cast in terms of seismicity rate changes.

[18] Our focus on dynamic deformations is motivated in part by the long distances between triggering and triggered earthquakes observed by *Felzer and Brodsky* [2006] and earlier studies of remote triggering (see also summaries of *Freed* [2005], *Steacy et al.* [2005], and *Hill and Prejean* [2007]), evidence for dynamic triggering at shorter distances [*Gomberg et al.*, 2003; *Pollitz and Johnston*, 2006], and because we can perform these tests using actual observations. Note that *Felzer and Brodsky* [2006] showed that, at least in the far-field, static stress changes and the *Dieterich* [1994] frictional triggering model are inconsistent with the aftershock densities. However, our goal is not further evaluation of static stress changes but instead, exploration of the role of dynamic deformations. Observations of dynamic deformations, or at least proxies for them, come from abundant seismic stations.

5.1. Justification for a Linear Relationship Between Dynamic Triggering Deformations and Probabilities

[19] The specific hypothesis we test is that, whatever the specific characteristic of the dynamic deformation considered, the probability that it triggers an earthquake is simply proportional to its value. No predictive quantitative models of the underlying physical mechanism of dynamic triggering have been proposed and thus, no guidance exists as to what form a more complex relationship should take. For example, even the well-vetted frictional model of *Dieterich* [1994] that explains seismicity rate changes as a response to static stress changes fails to predict both the temporal and spatial decay rates of dynamically triggered aftershock sequences [*Gomberg*, 2001; *Felzer and Brodsky*, 2006]. We therefore invoke Occam's razor, adopting the simplest assumption of proportionality as a reasonable, first-order place to start.

[20] The reasonableness of a linear relationship may be justified in several other ways. A number of observational studies have demonstrated qualitatively a dependence of triggering potential on deformation amplitude for both dynamic and static deformation triggering (see references in the work of *Hill and Prejean* [2007]). More recently, several studies infer a linear relationship between aftershock rates and transient afterslip based on the similarity between the temporal variations of measured post-main shock time-dependent displacements, measured aftershock decay rates, and theoretical models of various deformation mechanisms [*Perfettini and Avouac*, 2004, 2007; *Savage and Yu*, 2007; *Savage et al.*, 2007a, 2007b].

[21] Finally, the similarity between the scaling with r and D in our model of triggering probability inferred from the aftershock densities and that expected for seismic radiation from a finite fault (see Appendix B) seems an unlikely coincidence, suggesting a causal, approximately linear relationship between the two.

5.2. Characterizing and Measuring Dynamic Deformations

[22] We measured characteristics of seismic wave displacements, velocities, and accelerations. Velocities have been shown to be accurate proxies for dynamic strains [*Love*, 1927; *Jaeger and Cook*, 1979; *Gomberg and Agnew*, 1996], and cyclic strain amplitude is often considered as the independent variable in laboratory observations and theoretical models of dynamic nonlinearity and weakening developed by physicists (see *Johnson and Jia* [2005] and *Savage and Marone* [2008] for a review). Accelerations are proxies for strain rates (since velocity is proportional to strain). We examine both peak values of displacement (PGD), velocity (PGV), and acceleration (PGA) by themselves and measures of cumulative deformation over some duration. The importance of duration in failure processes has been noted in geotechnical and other engineering studies of dynamic deformation (e.g., of cyclic fatigue, soil nonlinearity due to shaking). For example, liquefaction potential due to strong shaking (i.e., extreme nonlinearity [*Snieder and van den Beukel*, 2004]), and crack growth due to cyclic fatigue [*Hertzberg*, 1995] show a dependence on the number of loading cycles. Although not definitive, studies of dynamic nonlinearity in rock and granular materials indicate that weakening increases with the number of cycles [*Johnson and Jia*, 2005; *Savage and Marone*, 2008].

[23] One measure of cumulative deformation we examined is the product of the peak deformation and the rupture duration. We assume that a rupture propagating across a finite fault occurs as a series of radiating subevents that all fail over a duration D/V_r, with rupture velocity, V_r, that is relatively constant among most earthquakes. Thus rupture duration is proportional to D. As a result when rupture duration is considered to be consistent with triggering probabilities (equation (8)), the peak deformation must scale as D rather than D^2. This perspective implies that the higher-frequency radiation is most significant for triggering, consistent with studies that show high-frequency radiation per unit rupture area is the same for moderate to great earthquakes [*Frankel*, 2006]. This also is consistent with the study of *Hanks and McGuire* [1981], who suggest that peak accelerations scale with the rupture duration because "larger earthquakes have larger peak accelerations only because they last longer, not because they are intrinsically more powerful." This type of cumulative deformation is particularly sensible to investigate since our relationships indicate that aftershock production is also a constant per unit rupture area.

[24] Another cumulative measure of deformation that may be considered is the integral or sum of deformations over the duration of the wave train rather than the duration of the rupture source. This cumulative measure also should scale with rupture dimension but decay more slowly with distance than the peak deformation averaged over the rupture dimension. The slower decay reflects the fact that, while the amplitudes decrease with distance, the duration increases. Additionally, surface wave dispersion and scattering produces a much longer duration than the source

Table 2. Published Attenuation Relation Parameters[a]

	m		*b*		*q*		*R*	
Reference	PGA	PGV	PGA	PGV	PGA	PGV	PGA	PGV
1	$(3.9-0.404M)$ $(2.5 \le M \le 6.3)$ 1.36 to 2.89	$(4.1-0.386M)$ $(2.5 \le M \le 6.3)$ 1.67 to 3.14	0	0	$(1.56-0.00376M^3)$ 0.62 to 1.50	$(1.42\ -0.00355M^3)$ 0.53 to 1.37	$r_e^2 + 8.9^2$	$r_e^2 + 7.3^2$
2	0.612	0.91	0	0	0.5	0.5	$r_s^2 + 5.8^2$	$r_s^2 + 3.6^2$
3	0.458	0.98	0	0	0.664	0.72	$r_j^2 + 7.27^2$	$r_j^2 + 7.06^2$
4	2.0	2.2	0.0032	0.0027	0.5 or 0.35	0.5 or 0.35	r_h^2	r_h^2
5	0.62	1.16	0.0032	0.0027	0.5 or 0.35	0.5 or 0.35	r_h^2	r_h^2
6	1.26	1.58	0.0031	0.0010	0.66	0.71	$(r_h + .96)^2$	$(r_h + .88)^2$
7	1.162	1.62	0.00414	0.00268	0.5	0.5	$(r_r + .00871D)^2$	$(r_r + 0.00871D)^2$
8	1.18	1.42	0.0039	0.0023	0.5	0.5	$r_r^2 + 0.0075D^2$	$r_r^2 + 0.0075D^2$
9	1.12	1.40	0.0031	0.0009	1.0	1.0	$r_r + 0.0055*D^{.74}$	$r_r + 0.0022*D^{.64}$
10	0.434	0.6	0	0	$0.53-0.0425M$	$0.504-0.0425M$	$r_r^2 + 5.6^2$	$r_r^2 + 4.0^2$

[a]Parameters used in published attenuation relations, following equation (9). Distance measures vary, with r_j = closest horizontal distance to the vertical projection of the rupture (Joyner-Boore distance), r_r = closest distance to the rupture surface, r_h = hypocentral distance, r_e = epicentral distance, and r_s = closest distance to the surface projection of the rupture surface [*Abrahamson and Shedlock*, 1997]. References: 1, *Bragato and Slejko* [2005]; 2, *Sabetta and Pugliese* [1987]; 3, *Pankow and Pechmann* [2004]; 4, *Boatwright et al.* [2003] M ≤ 5.5; 5, *Boatwright et al.* [2003] M > 5.5; 6, *Liu and Tsai* [2005]; 7, *Wu et al.* [2001]; 8, *Garcia et al.* [2005]; 9, *Kanno et al.* [2006]; 10, *Campbell and Bozorgnia* [2007] for $M \le 5.5$, and for $M > 5.5$ the power D is scaled by becomes a function of M equal to $0.434-0.46(M\text{-}5.5)$ or $0.6-0.268(M\text{-}5.5)$ for $5.5 < M < 6.5$ and $0.434-0.46(M\text{-}5.5)-0.228(M\text{-}6.5)$ or $0.6-0.268(M\text{-}5.5)-0.0166(M\text{-}6.5)$ for PGA and PGV, respectively.

rupture and is a prominent feature of the wave train in the far-field. We describe how we measure these cumulative deformations in Appendix C.

[25] We investigate the dynamic deformations both by using our own direct measurements from seismic data and by using published attenuation relationships, as described in the next sections. Seismic source and wave propagation theory also provide some expectations of how the ground motion characteristics we measure may vary with D and r. Indeed, they suggest a similarity with the scaling implied in *P(r, D)* and thus that our hypothesis warrants testing. However, theoretical models constrain the temporal or spectral characteristics of highly simplified sources and wavefields that do not precisely relate to our measurements of time domain peak deformations or cumulative deformations. We discuss this further in Appendix B.

5.3. Published Attenuation Relations

[26] Relevant published attenuation relations relate measurements of *PGA* and *PGV* to some measure of the distance and magnitude M (or D) via an equation of the form

$$pk(r,M) = 10^k 10^{\frac{m}{2}M} 10^{-br} R^{-q} = \qquad pk(r,D) = 10^k D^m 10^{-br} R^{-q} \tag{10}$$

where k, b, and q are empirical constants. The terms in most attenuation relations have some rooting in theoretical descriptions of seismic wave radiation and propagation, with 10^{-br} describing anelastic dissipation and scattering ($b \sim 0$ in many cases), R^{-q} describing geometric spreading, and D^m describing the dependence on rupture size (see Table 2). The probabilities of equation (8) predict scale changes around distances $r \sim D$ and possibly at $r \sim h$. These are included in many attenuation relations in various ways but usually as a single parameter within the single function R. For example, R may equal $r^2 + \delta^2$ in which δ is a fit constant interpreted as an average hypocentral depth (see Table 2).

[27] We discuss two sets of recently developed attenuation relations most relevant to this study. The relations of *Kanno et al.* [2006] are based on data from the same HiNet network in Japan that we have used data from and these authors measure distance similarly (see section 5.4.1 below), although for mostly larger earthquakes (Mw ≥ 5.5) and for r from 1 to 200 km. *Kanno et al.* [2006] describe *PGA* or *PGV* as

$$pk(r,D) = 10^k \frac{D^m}{(aD + r)} e^{-2.303br} \tag{11}$$

with $k = -1.93$, $m = 1.4$, $\alpha D = 0.0022 \times 10^{M/2}$, $b = 0.0009$ for PGV and $k = -1.93$, $m = 1.412$, $\alpha D = 0.0055 \times 10^{M/2}$, $b = 0.0031$ for PGA. The scaling with D, or m, differs from $m \sim 2$, and while perhaps consistent with the far-field distance scaling of *P(r, D)*, it does not fit well in the near field (Figure 4a).

[28] We also examine the *PGA* and *PGV* relations of *Campbell and Bozorgnia* [2007], developed as part of the NGA earthquake hazard study (*Power et al.* [2008]; see also http://peer.berkeley.edu/lifelines/nga.html), because we also use the same NGA data ourselves (section 5.4.2). *Campbell and Bozorgnia* [2007] use observations from the NGA database for earthquakes with M > 4.0 recorded out to 200 km, although there are few for M ≤ 5.5 earthquakes particularly at distances less than 10 km. The *Campbell and Bozorgnia* [2007] relations may be written as

$$\begin{aligned} p(r,D) &= 10^k \frac{D^m}{(d^2 + r^2)^{(n+2c\log D)}} \quad M \le 5.5 \\ &= 10^k \frac{\xi(D)}{(d^2 + r^2)^{(n+2c\log D)}} \quad M > 5.5 \end{aligned} \tag{12}$$

We denote their more complex scaling with rupture dimension at larger magnitudes by *ξ(D)* (Figure 4b). For $M \le 5.5$, their scaling with D depends on distance, varying from $m = 0.8$ and $m = 0.7$ at 0 km to $m = 1.4$ and $m = 1.2$ at

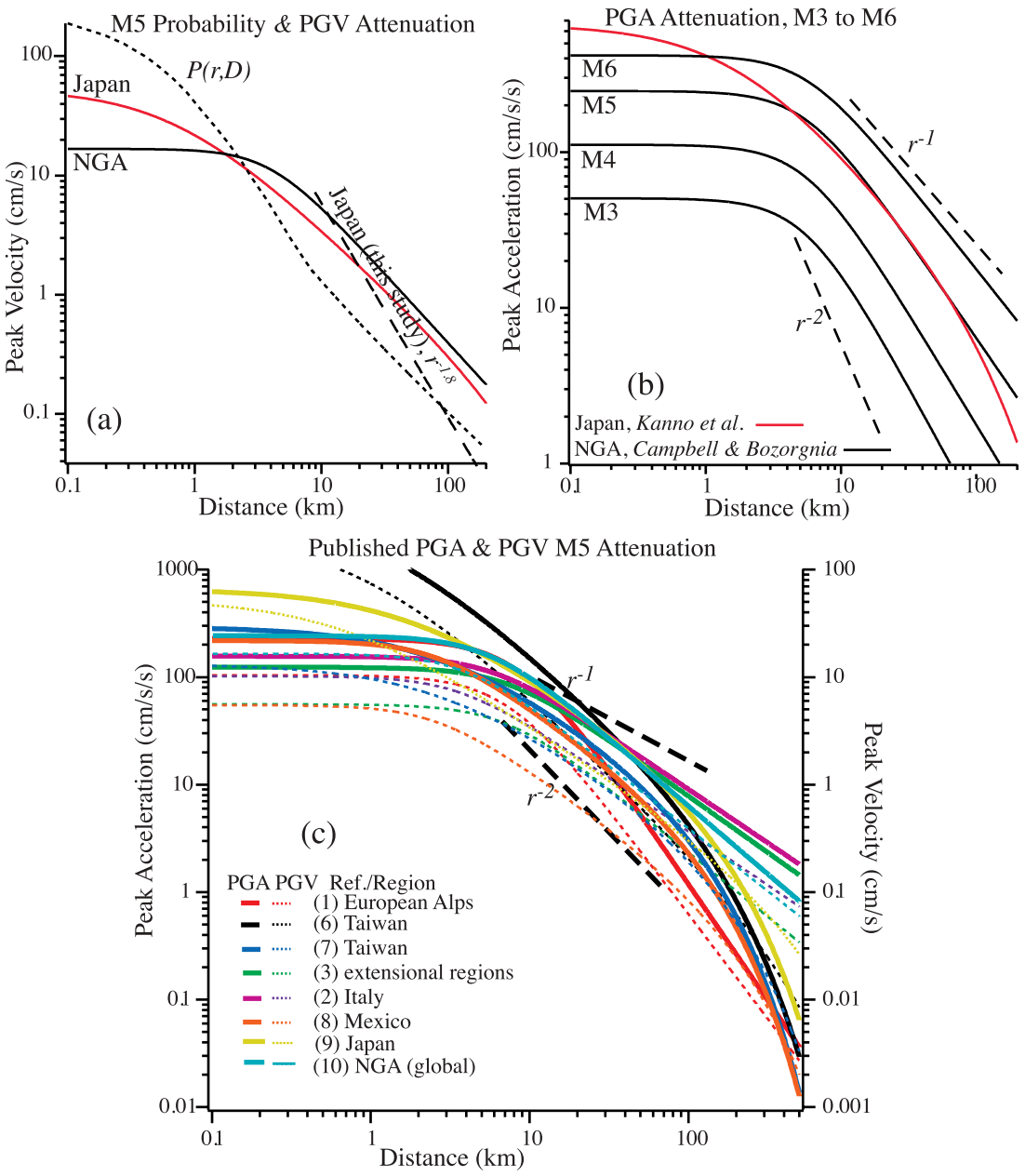

Figure 4. (a) Peak ground velocity (PGV) attenuation relations (solid curves) for a M5 earthquake constrained by HiNet data from Japan (red) published by *Kanno et al.* [2006] and by the global Next Generation Attenuation (NGA) data set published by *Campbell and Bozorgnia* [2007] (black). Theses have comparable decay rates in the far-field beyond ~8 km, to one another and to triggering probabilities scaled arbitrarily to *PGV* (dotted curve), but all differ in the near field. (b) NGA PGA attenuation relations (solid black curves) that have distance decay rates that change with magnitude (compare with dashed lines describing two power law decay rates). As for PGV, the *Kanno et al.* [2006] relation for Japanese earthquakes is similar in the far field but not in the near field. (c) Published attenuation relations for peak ground acceleration (*PGA*, left axis) and peak ground velocity (*PGV*, right axis). References numbered in the legend are listed in Table 2. Although plotted together, the distances in many of these are measured differently (see text and Table 2).

200 km for *PGV* and *PGA*, respectively. These all differ significantly from the value in *P(r, D)* for peak value alone (*m* must be ~2), but *PGA* averaged over the rupture duration is consistent (*m* must be ~1). The *Campbell and Bozorgnia* [2007] relations predict that the far-field distance decay rate increases as magnitude decreases; i.e., for *PGV* the relation varies from $\sim r^{-1.2}$ to $\sim r^{-1.5}$ and for *PGA* from $\sim r^{-1.1}$ to $\sim r^{-1.6}$ for M6 to M3, respectively (Figure 4b). The lower values compare well with the *h*-dependent form of *P(r, D)*.

[29] We also examined relations published in seven other recent studies (Figure 4c and Table 2). While sharing similarities with *P(r, D)*, a one-to-one parameter comparison is difficult to make for any of them. One reason is because the distance dependent term R typically does not have separate terms accounting for h and D, and r is measured in a variety of ways [*Abrahamson and Shedlock*, 1997]. Moreover, observational or model uncertainties on the fit parameters are not generally provided. Qualitatively, *PGA* is inconsistent with the $\sim D^2$-scaling (*i.e.*, $m \sim 2$) required if we are testing the peak values alone, but may be consistent with the D-scaling (i.e., $m \sim 1$) required if testing the product of peak value and rupture duration. *PGV* relations may be consistent with $m \sim 2$. The distance decay is more difficult to judge, particularly in the near field, but the far field decay rates for both *PGA* and *PGV* lie between r^{-1} and r^{-2}, which are the required rates for the h-dependent and h-independent *P(r, D)* probability models, respectively. Thus, we can only say that our hypothesis cannot be ruled out for either type of ground motion, *PGA* or *PGV*.

[30] If the hypothesis that the probability of triggering described by equations (8) is proportional to dynamic deformation characteristics is correct, as noted above, triggering deformations must decay more slowly as the fault is approached, and "saturate" (i.e., reach a limiting value next to the fault regardless of the size of the rupture). Both these features have long been recognized in the seismic hazard attenuation literature, although the question of saturation is still debated [*Anderson*, 2000; *Bragato*, 2005]. The most recent results of *McGarr and Fletcher* [2007] support saturation, evident in near-fault slip velocities measured from PGVs for earthquakes and mine failure events spanning orders of magnitude in size, laboratory experiments, and slip models that all converge to similar values. The NGA data discussed in the next section also show a decreasing decay rate as the fault is approached and convergence to a single value, which may be explained as a consequence of radiation from a finite rupture plane (see Appendix B and *Anderson* [2000]) and the requirements of simple models of rupture and seismic radiation [*Brune*, 1976].

5.4. Ground Motion Observations

[31] Our own data analysis perhaps should be viewed largely as illustrative, serving as guidance for future studies. The data we use come from many locations globally. A large portion of our dynamic deformation data come from two of the most densely monitored areas in the world, southern California in the United States and Japan, but despite the optimal coverage we found it possible only to measure far-field deformations for these. This is because the closest distances to the rupture planes of small to moderate magnitude earthquakes at typical hypocentral depths usually far exceeded their source dimensions. To examine near-field deformations requires data from either large, infrequent earthquakes that rupture near the surface or extraordinarily shallow, small earthquakes that occur near recording stations. The relative rarity of these types of earthquakes thus requires combining data from a variety of tectonic environments and instrumentation. Fortunately such a data set has been compiled for the NGA project and is publicly available. We examine the NGA data more qualitatively than for the other two data sets because of the greater heterogeneity of the regional structure, source and site conditions, etc. In this section we describe these data sets, the measured scaling with earthquake size and distance for each. In each case we test our hypothesis that each deformation measure is proportional to our model of triggering probability.

Table 3. Main Shock Source Parameters

Origin Time (year/month/day/hmin:s)	Epicenter (latitude, longitude)	Depth (km)	M	Name/ Location
	Japanese Earthquakes			
2005/02/08/2323:09	35.020, 132.788	7.0	3.0	
2005/02/05/0753:56	38.380, 141.170	10.0	3.1	
2005/01/18/125032	37.367, 139.000	8.0	4.7	
2005/01/01/1630:26	35.862, 137.580	6.0	4.2	
2004/12/28/0930:36	37.318, 138.985	8.0	5.0	
2004/12/14/0556:10	44.073, 141.703	9.0	6.1	
2004/11/06/1511:02	37.152, 138.740	11.0	3.0	
2004/10/27/0559:19	37.363, 138.937	11.0	4.2	
2004/10/25/0546:41	37.317, 138.885	15.0	3.7	
2004/10/25/0417:10	37.203, 138.830	10.0	3.0	
2004/10/24/0129:18	37.433, 138.930	15.0	4.1	
2004/10/04/2333:51	35.930, 136.380	12.0	4.8	
2004/09/04/0218:38	41.260, 140.820	14.0	3.8	
2004/07/26/1554:56	35.755, 137.110	11.0	4.5	
2004/07/09/1054:12	39.910, 141.040	9.0	4.4	
2004/06/07/2305:23	34.210, 135.080	8.0	4.5	
2004/06/03/1004:29	35.780, 137.550	7.0	3.2	
2004/05/08/1949:13	35.515, 136.280	11.0	3.4	
2004/03/14/1918:24	39.921, 139.978	15.0	3.7	
2004/03/03/0455:59	35.73, 137.05	13.0	3.7	
2004/03/02/0630:44	38.46, 141.21	12.0	3.4	
	California Earthquakes			
2005/06/12/15:41:46	33.529, −116.573	14.2	5.2	Anza
2005/06/16/20:53:26	34.058, −117.011	11.6	4.9	Yucaipa

5.4.1. Far-Field Scaling From Japanese and Californian Data

[32] From Japan we used ground motion data from the HiNet network operated by the National Research Institute for Earth Science and Disaster Prevention (NIED). This network includes over 700 stations, each with three-component, 100-m borehole, weak motion velocity seismometers. We measured ground motion characteristics for 22 Japanese earthquakes (Table 3) with magnitudes of M3.0 to M6.1 (Japanese Meteorological Agency magnitudes). We selected the shallowest, onshore events to minimize the source-station distances, and still almost all the ground motion measurements are in the far-field. For these data we use hypocentral distances because the rupture planes are not known for many of the earthquakes, noting that at these distances the difference between hypocentral and the closest distance to the rupture is insignificant. To estimate the scaling with rupture dimension D of the type of dynamic displacement that we are investigating we first correct all measurements to a reference magnitude $M = 5$ by multiplying it by $10^{(M-5)m/2}$, (which is the equivalent of multiplying by $D^{(M-5)m}$), for trial values of m from 0.2 to 4. We then compute a correlation coefficient between main shock magnitude and amplitude for each value of m. Finally we select the value of m that minimizes the correlation. The power law distance decay rate is estimated using a least squares fit to the corrected amplitudes. Uncertainties in both parameters represent 98% confidence intervals and are estimated using bootstrap sampling (1000 bootstraps per parameter value). Figure 5 and Table 4 summarize the

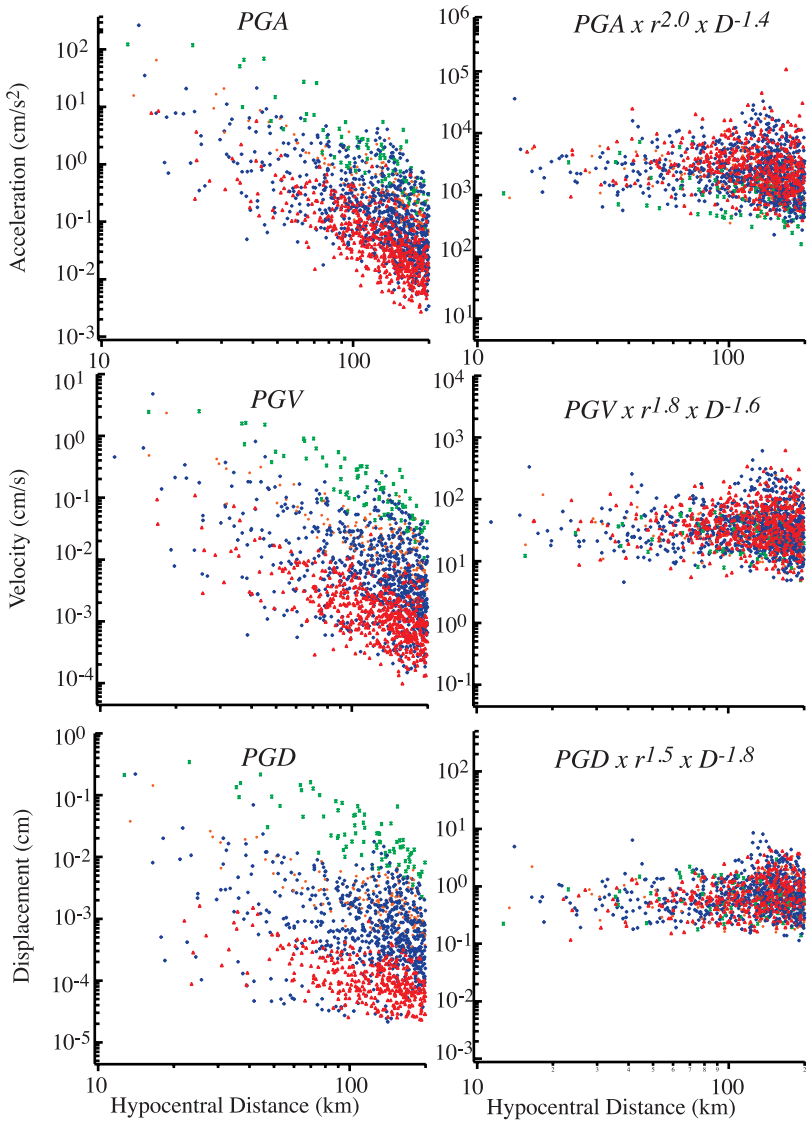

Figure 5. (left) Peak ground accelerations (*PGA*), velocities (*PGV*), and displacements (*PGD*) measured for 22 Japanese earthquakes (see Table 2) with $3.0 \leq M < 4.0$ (red), $4.0 \leq M < 5.0$ (blue), $5.0 \leq M < 6.0$ (orange), $6.0 \leq M$ (green) at HiNet seismic stations and plotted as a function of hypocentral distance, *r*. (right) We find the scaling parameters that best remove all dependence on *r* and rupture dimension, *D* (or equivalently, *M*), assuming a far-field scaling of D^m and a power law decay rate with *r*. When corrected for this scaling (see the text for the fitting procedure), the scatter for all the data together is comparable to that for any individual event.

scaling of peak displacements, velocities, and accelerations estimated for the HiNet data.

[33] The second data set includes ground motions for the 2005 M_w5.2 Anza and 2005 M_w4.9 Yucaipa earthquakes (Table 3) in southern California, measured from accelerograms recorded by California Geological Survey CSMIP, the U.S. Geological Survey NSMP, University of California, San Diego's (UCSD) Anza strong motion networks, and from broadband velocity seismograms recorded by UCSD's Anza network and the California Integrated Seismic Network. We chose these two earthquakes because of the abundance of data and well-characterized aftershock sequences [*Felzer and Kilb*, 2006]. The depths and sizes of these ruptures limit ground motion measurements to far-field distances of ~10 km and from two earthquakes we cannot estimate the scaling with *D*. However, we can measure the distance decay rate for all three deformation characteristics (Table 4, Figure 6).

[34] As a reminder, consistency with our hypothesis requires that the aftershock triggering deformations scale with distance from the fault as r^{-n} with $n \sim 2$ and with fault dimension as D^m with $m \sim 2$ if considering peak deformations alone and $m \sim 1$ if considering peak deformation averaged over the rupture dimension or cumulative deformations summed over the wave train. If *P(r, D)* changes at $r \sim h$ then the observed deformation will decay as $r^{-(n-1)}$ at $r > h$, which is the region in which the vast majority of our measurements are located. Our hypothesis also requires

Table 4. Measured Scaling Parameters[a]

Data Source	D Scaling	r Decay Rate Scaling, Peak Deformation	r Decay Rate Scaling, Cumulative Deformation	r Decay Rate Scaling, Duration
		California		
Acceleration		2.2 (±0.2)	1.7 (±0.4)	0.5 (±0.3)
Velocity		1.8 (±0.2)	1.1 (±0.4)	0.6 (±0.3)
Displacement		1.3 (±0.2)	0.8 (±0.6)	0.5 (±0.4)
		Japan		
Acceleration	1.4 (−0.1, +0.2)	2.0 (±0.2)		
Velocity	1.6 (−0.1, +0.2)	1.8 (±0.2)		
Displacement	1.8 (±0.1)	1.5 (±0.2)		

[a]The D scaling estimates are the estimated powers m of D^m in equation (8). The r decay rate scaling for peak or cumulative measurements are made at $r > D$ and $r > h$, so they correspond to n or $n - 1$ in the modeled far-field power law. We assume durations follow a power law increase with distance and report measured powers fit to durations (right column) estimated as part of the cumulative deformation measurement. All uncertainties represent 98% confidence levels.

that the aftershock triggering deformation converge to a magnitude-independent value near the fault surface.

[35] We have a sufficient range of event sizes to measure the scaling with D only for the Japanese data, and measure $m = 1.8 \pm 0.2$, 1.6 ± 0.2, $1.4 - 0.1 + 0.2$ for peak displacements, velocities (strains), and accelerations (strain rates), respectively (see Table 4). Thus we can rule out peak strain rates (consistency with *P(r, D)* requires $m \sim 2$), as well as peak strains and displacements averaged over the rupture dimension (consistency requiring $m \sim 1$). The latter also suggests that cumulative displacements and strains summed over the wave train may be ruled out, although this is based on our assumption that these cumulative measures scale similarly; we cannot verify this assumption because we have measured cumulative deformations over the wave train only for the two California earthquakes.

[36] We measure exponents of the power law distance decay rates of peak deformations for both the Japanese and California data and of cumulative deformations only for the California data. We obtain power law exponents of 1.5 ± 0.2 and 1.3 ± 0.2 for peak displacements, 1.8 ± 0.2 and 1.8 ± 0.2 for peak velocities (strains), and for peak accelerations (strain rates) 2.0 ± 0.2 and 2.2 ± 0.2, respectively (Table 4). (The standard Richter M_L relationship for short period seismic wave amplitude decay in California assumes a power law decay exponent of 1.2 [*Richter*, 1935], consistent with our measurements.) This increasing decay rate going from displacement, to velocity, and to acceleration is consistent with the findings of *Hanks and McGuire* [1981]. Cumulative deformations decay more slowly, with exponents of 0.8 ± 0.6, 1.1 ± 0.4, and 1.7 ± 0.4 for California recordings of displacement, velocity, and acceleration, respectively. These and the D scaling results indicate that peak strains, peak strain rates averaged over the rupture duration, or cumulative strain rates are proportional to *P(r, D)* in the far-field, assuming an h-independent *P(r, D)* model. Alternatively, if we assume *P(r, D)* depends on h, only peak displacements are proportional to *P(r, D)*.

[37] The distance decay rates we obtain for *PGA* and *PGV* are significantly greater than those estimated from published attenuation relations. We suggest several possible reasons for this. The similarity in our measurements with those for two earthquakes in the NGA data set from the same region (Figure 6) suggests that the difference is not due to some measurement bias but rather to the choice of functional form fit to the data. We fit a single, simple power law to the data from the entire distance range of ~10 to 100 km, noting that statistical tests showed that fitting a more complex function than a single power law was not warranted. The relatively greater abundance of data sampling distances > ~40 km, where attenuation should be more significant, may bias the estimate toward values higher than what may be appropriate at shorter distances (K. Campbell, personal communication, 2008), noting that the published relations are derived by fitting more complex functions and focus on fitting observations at distances < ~40 km where potential damage is more likely and attenuation may be less significant. While running through the median of the data for most distances our fit relation appears qualitatively to overpredict the median value at distances less than ~30 km. Another possible reason for our steeper decay rates is that the magnitudes of the events we consider, particularly in the Japanese data set, are smaller than those generally examined in published studies, which focus on earthquakes with M > ~5. The *Campbell and Bozorgnia* [2007] attenuation relations predict faster decay rates with decreasing magnitude, implying that perhaps the more rapidly attenuating higher frequencies are more dominant in determining the *PGA* or *PGV* of smaller earthquakes.

5.4.2. Near- and Far-Field Scaling From Global Data

[38] The publicly available NGA data set of *PGD*, *PGV*, and *PGA* measurements allows us to examine scaling at both near- and far-field distances. We selected NGA data for those earthquakes for which the closest distance to the fault and estimates of the rupture area also exist in the database, resulting in a subset of observations for events with M > 5.5 recorded between 0.07 and 200 km. This data set is similar to that that for *PGV* only presented by *Gomberg and Johnson* [2005] but is more complete and measurements were made more uniformly. Key features of the NGA data are the decreasing decay rate as the fault is approached at distances less than $r \sim D$ and the convergence of *PGV*s to an approximately constant value regardless of source size as $r \rightarrow 0$ (Figure 7). The inferred triggering probabilities, *P(r, D)*, share these same features, suggesting the two are proportional and causally related as hypothesized (see the end of section 4).

[39] To examine the scaling of the NGA data easily from the near- to far-fields we normalize the distances using $\tilde{r} = r/D$. The transition from near- to far-fields occurs at many different distances for a data set containing a large range of rupture dimensions (Figure 7a), but for this scaled

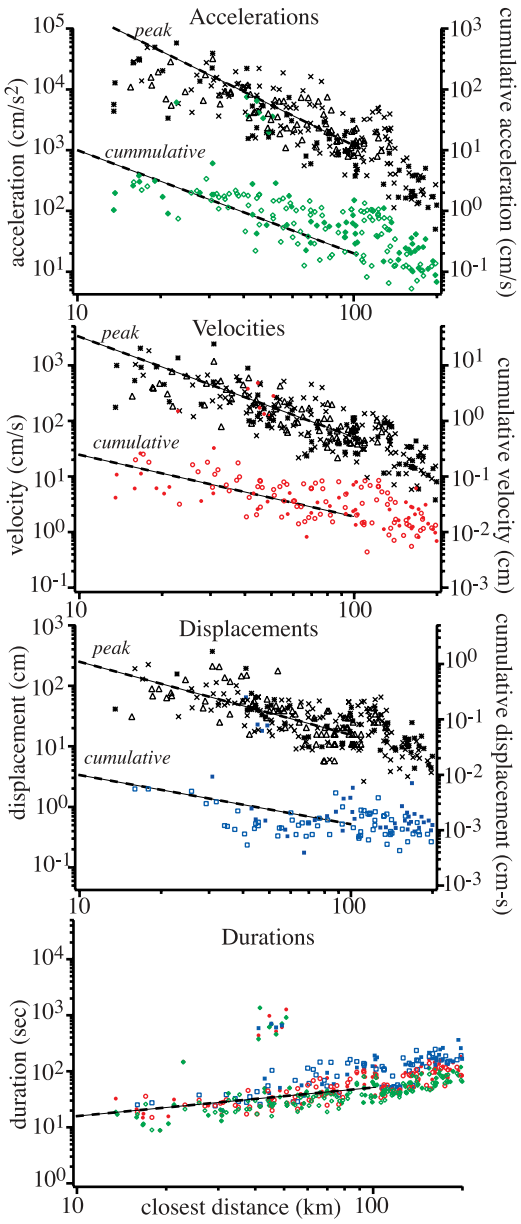

Figure 6. Measured peak deformations (left axis) for the M5.2 Anza (asterisks) and M4.9 Yucaipa (crosses), California earthquakes and cumulative deformations (left axis) for the corresponding earthquakes (solid and open symbols, respectively). Measurements for M5.2 and a M4.9 Anza-region earthquakes in 1980 and 2001, respectively, from the NGA database are also shown (triangles). All measurements have been scaled to a magnitude M5.2 assuming the same scaling with D measured for the Japanese earthquakes. Power law decay rates were fit to the measurements we have made from 10 to 100 km (dashed lines). (bottom) Also shown are the durations estimated as part of the cumulative deformation measurement (coded identically as the latter). Durations increase with distance nearly identically regardless of the motion type; this increase explains the slower decay rate of the cumulative deformations relative to the peak values because the former depends on both the duration and peak amplitude.

distance the transition occurs at $\tilde{r} \approx 1$ regardless of the earthquake's size and $\tilde{r} \ll 1$ or $\tilde{r} \gg 1$ corresponds approximately to the near- or far-fields, respectively.

[40] Our hypothesis test compares the data with the inferred probability model, *P(r, D)* (equation (8)). For most of the earthquakes in the NGA database the ruptures are large enough that $h = 0$. When $h = 0$ and using the scaled distance, the probability becomes

$$\frac{D^{m-n}}{(\alpha+\tilde{r})^n} \text{ or } \frac{D^{m-n}}{(\alpha+\tilde{r}^n)} \tag{13a}$$

assuming *P(r, D)* does not change at h. If *P(r, D)* does change at h then the equation becomes

$$\frac{D^{m-n}}{(\alpha+\tilde{r})^n}(\tilde{r}+1) \text{ or } \frac{D^{m-n}}{(\alpha+\tilde{r}^n)}(\tilde{r}+1) \tag{13b}$$

In both cases consistency with our hypothesis requires that $m \sim n \sim 2$ if considering peak values alone or $m \sim 1$ *and* $n \sim 2$ for peak values averaged over the rupture duration.

[41] The above requirements imply that if the peak values are consistent with our hypothesis then no dependence on D should exist when data are plotted as a function of $\tilde{r}$. In Figures 7b–7d we plot the NGA *PGDs*, *PGVs*, and *PGAs* in terms of $\tilde{r}$, and find qualitatively that only *PGV*s become independent of D. This suggests that for peak values, only strains are proportional to our triggering probability model. Similarly, if the hypothesis is correct for peak values averaged over the rupture duration, then the D-dependence should vanish for plots of peak values divided by the corresponding D. This appears true for strain rate, evident in plots of *PGAs* divided by the appropriate D versus $\tilde{r}$ (Figure 7e). Figure 7c shows that for *PGD*s $m > n$, suggesting that both peak displacements alone or averaged over the rupture duration are inconsistent with our hypothesis.

[42] The NGA data are consistent with our hypothesized proportionality with *P(r, D)* and narrow the possible deformations (i.e., eliminating peak displacements), indicating triggering deformations must be either peak strain or peak strain rate averaged over rupture duration. (The NGA data provide no constraint on the cumulative deformations summed over the wave train.) This is consistent with inferences from the Californian and Japanese data and the h-independent model of *P(r, D)*.

6. Discussion

[43] A primary goal of this study was to develop a model of how triggering probabilities scale with distance from and the rupture dimension of a triggering main shock. Such a model can then be used to test hypotheses about the triggering potential of specific deformations, which can be measured or modeled. This is important for evaluating physical models of dynamic weakening and nucleation [*Beeler and Lockner*, 2003, *Brodsky and Prejean*, 2005, *Johnson and Jia*, 2005] and for applications that use probabilities directly (see below). In Figure 8a we show examples of how the probability of triggering a single aftershock varies with distance for hypothetical main shocks

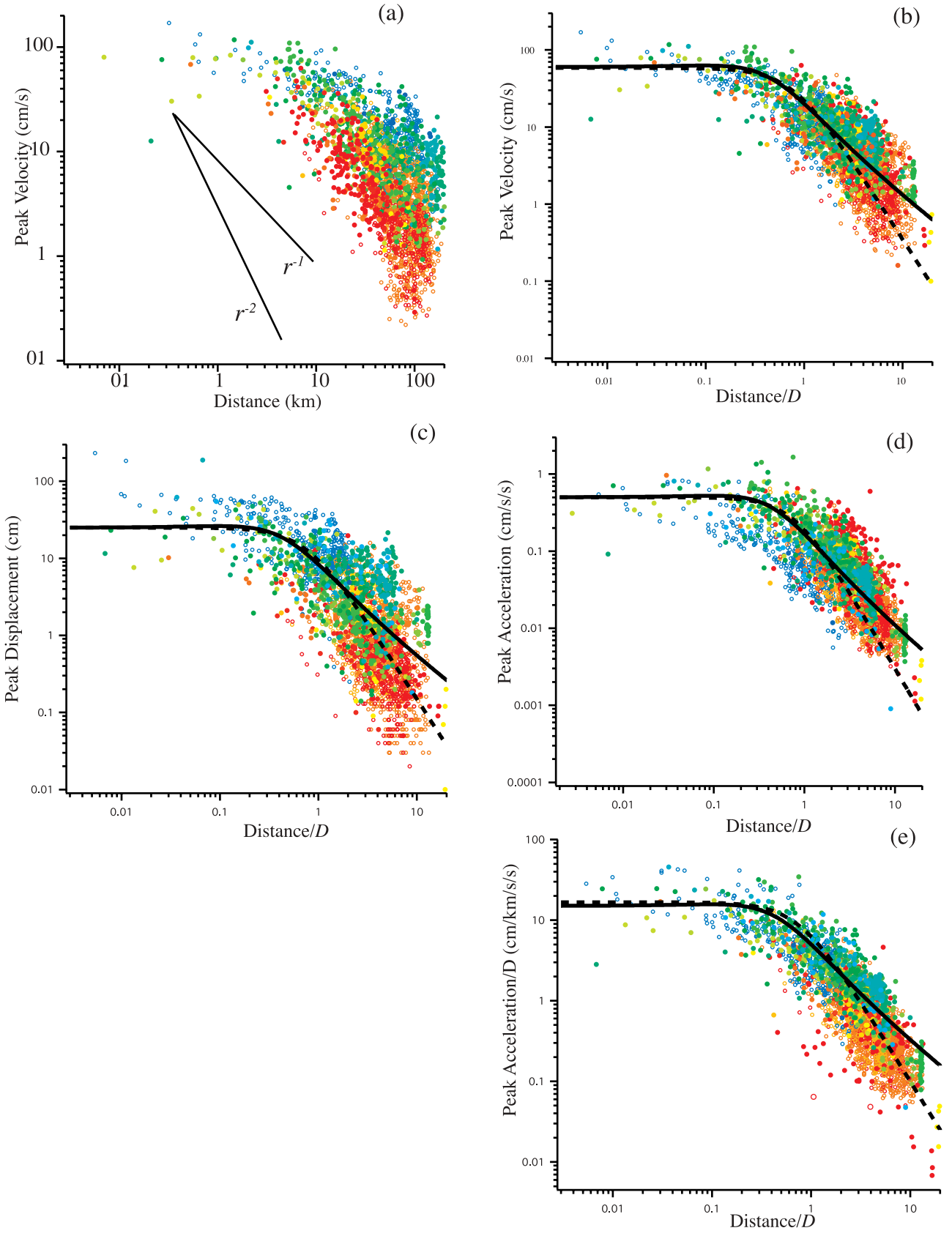
(a)
Peak Velocity (cm/s)
100
10
1
01
01
1
10
100
Distance (km)
r^{-1}
r^{-2}
(b)
Peak Velocity (cm/s)
100
10
1
0.1
0.01
0.01
0.1
1
10
Distance/D
(c)
Peak Displacement (cm)
100
10
1
0.1
0.01
0.01
0.1
1
10
Distance/D
(d)
Peak Acceleration (cm/s/s)
1
0.1
0.01
0.001
0.0001
0.01
0.1
1
10
Distance/D
(e)
Peak Acceleration/D (cm/km/s/s)
100
10
1
0.1
0.01
0.01
0.1
1
10
Distance/D

Figure 7

of various magnitudes. Note that the probabilities very close to the fault are the same regardless of main shock magnitude. Away from the main shock fault aftershock triggering probabilities at a point depend on the rupture dimension such that for small to moderate magnitudes, by a distance equal to ~1 rupture dimension probabilities have decreased to 10 to 20 percent of the maximum. For larger magnitudes and distances the probabilities decay more slowly and may change scale from $\sim 1/r^2$ to $\sim 1/r$.

[44] Linear aftershock densities also describe probabilities but of a different type; i.e., they describe the likelihood of an aftershock occurring at a given distance at any azimuth surrounding the triggering fault. That is, instead of describing the probability of an aftershock occurring at a point, linear aftershock densities describe the rate of aftershocks in an annulus surrounding the fault. In this case, the relative probability (that normalized by the total number of aftershocks for a given earthquake) falls off at a constant rate with distance, without any change of scale associated with the rupture dimension. In other words, while the probability of observing a single aftershock at some distance from a main shock of magnitude M scales with the total number of aftershocks or as $10^M \sim D^2$, the change in probability with distance is the same regardless of M (Figure 8b).

[45] The ability to estimate both types of probabilities has practical applications for time-dependent earthquake forecasting. For example, real time maps of earthquake ground motions, i.e., dynamic deformations, are now routinely produced for moderate and large earthquakes. The results of this case study suggest that a map of *PGV*s perhaps could be used directly to estimate the likelihood of an aftershock occurring at a specific location on the map using the first type of probability or anywhere at a given distance using the second.

[46] We comment only briefly on the implications for static stress triggering because *Felzer and Brodsky* [2006] already have shown that the hypothesis that static stress changes trigger aftershocks at short times can be rejected, if one assumes that static stress change leads to aftershock occurrence via the nonlinear rate and state friction model described by *Dieterich* [1994]. Static stress change can also be rejected as the trigger if a linear relationship between stress amplitude and triggering is assumed, noting that numerical calculations show that far-field static stresses decay more rapidly than dynamic stresses by $\sim 1/r$ [*Cotton and Coutant*, 1997] and theoretical static stresses from a dislocation source decay as $1/r^3$ [*Helmstetter et al.*, 2005]. Both the nonlinear and linear far-field static stress changes decay too fast to be consistent with the triggering probabilities we infer. This decay is faster than the power law exponent of $n = 2$ that we infer for a linear triggering relationship.

7. Summary and Conclusions

[47] We have developed a model of how the probability of triggering an aftershock scales with distance, r, and main shock magnitude or equivalently rupture dimension, D, based on observations of linear aftershock densities. Specifically, we find that triggering probabilities in the far-field ($r >> D$) are proportional to D^m with $m \sim 2$ and become independent of D as r approaches zero. The distance scaling requires that in the far-field triggering probabilities decay with distance approximately as r^{-n} with $n \sim 2$, with a possible change to $r^{-(n-1)}$ at $r > h$. (h is the distance from the edge of the rupture plane to the top or bottom of the seismogenic zone.) All these features are embodied mathematically in equations (8).

[48] The inferred probability model may be used to test hypotheses about posited triggering deformations and their potential to trigger. As an example we have hypothesized that triggering probabilities are proportional to various characteristics of dynamic deformations. We examined three types of dynamic deformations; displacements, velocities (strains), and accelerations (strain rates). For each of these we measured peak deformations, peak deformations lasting the duration of rupture, and cumulative deformations summed over the duration of the wave trains. The latter two measures of accumulated deformation differ in that the first depends only on the rupture process and the later also includes the affects of propagation, which spreads the deformations over durations that generally increase with distance.

[49] Two of the three data sets we examined sample a single region; Japan for 22 mostly small earthquakes and southern California for two moderate, M~5, earthquakes. For these we measure peak and cumulative deformations from seismic data, which are available only at far-field distances. Our analysis of the Japanese and Californian data sets yields peak value distance decay rates that exceed most published values, probably because we fit a single decay rate at all distances and because we sample smaller magnitude earthquakes. The third data set samples deformations at near- and far-field distances from global M > 5.5 earthquakes taken from the NGA database. From these three data sets we find that only peak strains or peak strain rates averaged over the rupture duration scale with distance and rupture dimension in the same way as the inferred probability model, *P(r, D)*, that has no dependence on the

Figure 7. Peak ground motion measurements from the NGA database for 5.5 < M < 7.9 earthquakes globally recorded between 0.07 and 200 km. Symbols are color coded so colors change from red to yellow, orange, green, and blues as magnitudes increase. Curves on each are qualitative fits of the functional forms $(1 + r)/(0.2 + r^2)$ (solid) and $1/(0.6 + r^2)$ (dashed) expected if peak deformations are proportional to triggering probabilities that assume h-dependent *P(r, D)* and h-independent *P(r, D)* models, respectively. (a) Peak velocities (PGVs) plotted as a function of the closest distance to the fault. (b) The same measurements in Figure 7a but now as a function of r/D. Estimates of D are also from the NGA database. (c) The same measurements in Figure 7b but for peak displacement or PGD. (d) The same measurements in Figure 7b but for peak acceleration or PGA. (e) PGA measurements scaled by D estimates and plotted as a function of r/D. See text for explanation.

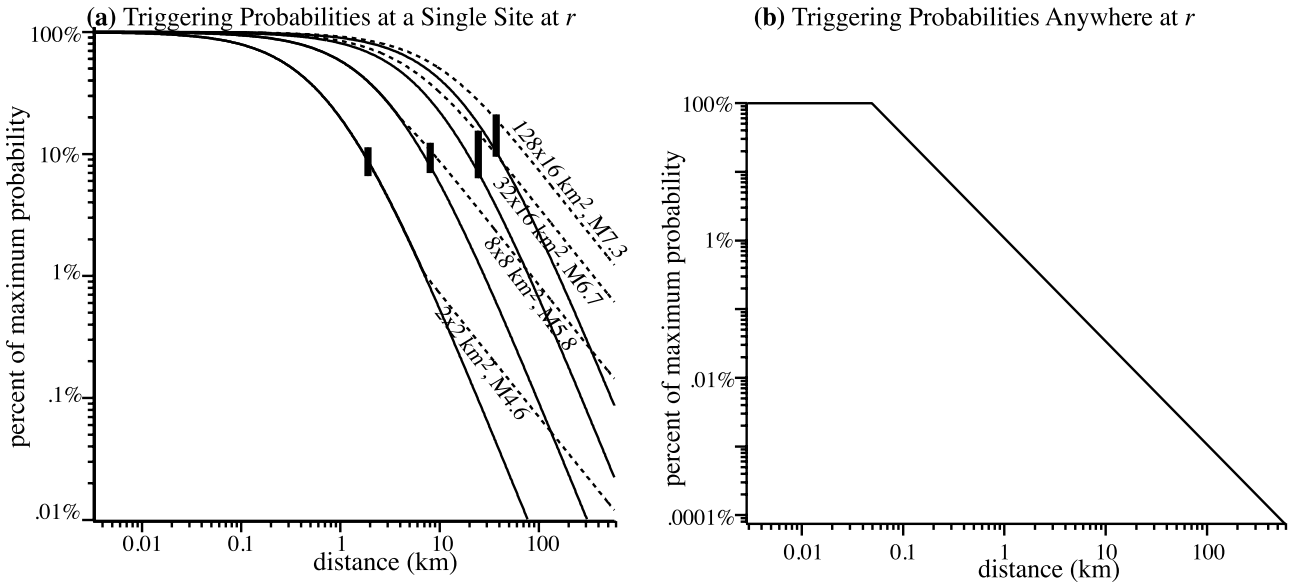

Figure 8. Theoretical curves describing the probability of triggering and its variation with distance and magnitude. (a) Probabilities describing the potential to trigger an individual fault at a particular distance, calculated according to equation (8) (solid, *h*-independent *P(r, D)* model; dashed, *h*-dependent *P(r, D)* model) with $\alpha = 0.4$, $m = n = 2$ for hypothetical triggering earthquakes with rupture dimensions or magnitudes labeled; we assume here that $D \sim 1$ km for a M4 main shock and D^2 is proportional to 10^M. Although the absolute value of the probability at $r \sim 0$ is not known, it converges to the same maximum value at $r = 0$ regardless of earthquake size and decrease rapidly at the point of maximum curvature at $r = \alpha D/2$. Thick vertical bars on curve(s) for each magnitude indicate distances corresponding to one rupture dimension. (b) Theoretical aftershock densities describe the total number of aftershocks expected at a particular distance (calculated here for $\gamma = 1.5$ with a constant density at $r < 50$ m). The maximum density occurs next to the rupture and is proportional to 10^M or D^2, and corresponds to the maximum probability. The absolute probabilities scale as 10^M but change with r identically regardless of M or D; e.g., for every $\Delta M = 1$, ten times more aftershocks are expected at all distances.

boundaries of the seismogenic zone. Future work should investigate the physical mechanisms by which these deformations may lead to aftershock triggering.

Appendix A: Scaling Uncertainties

[50] To quantify the allowable variability in the distance scaling term n in *P(r, D)* we look at the ratio, *R(r)*, of the observed to modeled densities, which should vary with r within the uncertainties in γ in equation (2). In other words, the modeled densities should predict a distance decay rate that approximates the power law $r^{-\gamma \pm \Delta\gamma}$. If this is true, then

$$\left|\frac{d \ln R}{d \ln r}\right| = \left|\left(\frac{r}{R}\right)\frac{dR}{dr}\right| \le \Delta\gamma \tag{A1}$$

We use this to constrain permissible range of values of n.

[51] We derive the ratio *R(r)* using equations (6) and (8) and the requirement that $\gamma = 3\text{-}d$. We use a normalized distance $\tilde{r} = \frac{r}{D}$ so that the results are independent of main shock size, and for compactness define $\tilde{h} = \frac{h}{D}$. For the *h*-independent *P(r, D)* model *R(r)* can be written as

$$D^{(m-n)}\frac{\left[\tilde{r}^2 + \tilde{r} + \frac{1}{2\pi}\right]}{\left[\alpha + \tilde{r}^n\right]} \text{ or } D^{(m-n)}\frac{\left[\tilde{r}^2 + \tilde{r} + \frac{1}{2\pi}\right]}{\left[\alpha + \tilde{r}\right]^n} = \left(\frac{C10^{-M_{\min}}}{4\pi AK}\right)D^{\pm 2\varepsilon \pm \Delta\gamma} \quad \tilde{r}^{\pm\Delta\gamma} \tag{A2a}$$

For $r > h$ and the *h*-dependent *P(r, D)* model the numerators in square brackets differ; for example, the leftmost ratio above becomes

$$D^{(m-n)}\left[\frac{\tilde{h}}{\tilde{r}}\tilde{r}^2 + \tilde{r}\left\{1 + \frac{1}{\pi}\cos^{-1}\left(\frac{\tilde{h}}{\tilde{r}}\right)\right\} + \frac{1}{2\pi}\right]\frac{(\tilde{r}+1)}{2[\alpha + \tilde{r}^n][\tilde{h}+1]} = \left(\frac{C10^{-M_{\min}}}{4\pi AK}\right)D^{\pm 2\varepsilon \pm \Delta\gamma} \quad \tilde{r}^{\pm\Delta\gamma} \tag{A2b}$$

K is a proportionality constant between the triggering deformation and corresponding probability. We plot examples of $\Delta\gamma(r)$ calculated according to equation (A1) in Figure 3c. These suggest that variations in n of less than about ±0.2 would result in aftershock density decay rates that could be fit with a constant power law with variability in decay rate of $\Delta\gamma \sim 0.2$ in the far-field and less in the near-field. Larger variations are implied near $r \sim h$ due to the simplicity in how *P(r, D)* changes scaling at this distance (i.e., by including a multiplicative factor of r/h), but we suggest that a more complex model is not warranted since our goal is to model the statistical properties of many main shock-aftershock sequences with differing values of h. In addition, the calculations shown in Figure 3c do not account for modeling uncertainties (e.g., in *F(r)*, etc.), so while variations in n of ±0.2 slightly underpredict and overpredict

the observational uncertainties of $\Delta\gamma\sim0.3$ and $\Delta\gamma\sim0.1$ km^{-1} in the near- and far-field, respectively [*Felzer and Brodsky*, 2006], they provide reasonable approximate estimates to use when evaluating the consistency of measured values of n with our model of $P(r, D)$.

[52] We also consider the allowable variability in the scaling of $P(r, D)$ with D, given the observational uncertainties. Equalities (A1) are only satisfied if $m\sim n$ within $\sim2\varepsilon$ or $\sim10\%$, and thus consistent values in the range $\sim1.8 < m < \sim2.2$. (the factor $D^{\pm\Delta\gamma}$ comes from the distance normalization and thus, is not real uncertainty in the D-scaling).

Appendix B: Theoretical Justification for Seismic Deformation Scaling Relations

[53] Herein we review some basic seismic source and propagation theory to show that it is consistent with some of the features of the modeled triggering probabilities and to highlight the expected dependence on frequency content. In particular, we review the theory that shows that to first-order dynamic deformations should scale as D^m/r^n in the far-field and become independent of D very close to the fault. The scaling with fault dimension, D^m, may differ for displacements, velocities, and accelerations, with m decreasing for each, respectively. These features derive from the theory describing shear wave displacements radiated from a fault of finite dimensions, acknowledging that the true dynamic deformation field is much more complex (i.e., include interactions with the free surface and scatterers). Velocities or accelerations may be considered high-pass filtered versions of displacements.

[54] The complete displacement field at some position x due to rupture of a fault of finite area $\Sigma \sim D^2$ is often modeled as the sum of radiation from point dislocation sources [see *Motazedian and Atkinson*, 2005, and references therein], represented by the slip, $\Delta u(\xi, t)$, across infinitesimal fault surfaces of area $d\Sigma(\xi)$. The total displacement is the sum or integral of these. The scaling change with D and frequency content becomes apparent looking at the far-field shear wave displacement, $u(x,t)$, described by an equation of the form

$$u(x,t) \propto \iint_{\Sigma} \left\{ \frac{1}{r(x,\xi)} \dot{\Delta u}(\xi, \bar{t} \right\} e^{-\zeta r(x,\xi)} d\xi \qquad \bar{t} = t - \frac{r(x,\xi)}{V_s} \tag{B1}$$

[*Aki and Richards*, 1980; *Ben-Menahem and Singh*, 1981]. The ground displacement, $u(x, t)$, is the time derivative (indicated by the dot) of the fault displacement, Δu, integrated over the fault surface, with geometric spreading described by the inverse of the distance to the fault, $r(x, \xi) = |\boldsymbol{x}\text{-}\xi|$. V_s denotes shear wave velocity and the exponential term approximates anelastic losses. Expression (B1) may be rewritten, assuming (1) the slip is spatially uniform and evolves with time according to a source time function, $g(t)$, or

$$\Delta u(\rightharpoonup \xi, t) = \Delta u \times g(t) \tag{B2}$$

(2) that slip is related to the stress drop according to

$$\Delta\sigma \approx \mu(\Delta u/D) \tag{B3}$$

and (3) that the attenuation may be approximated as a power law with respect to r.

[55] The displacement may now be rewritten as

$$u(\rightharpoonup x,t) \propto \Delta\sigma D/r^{n'} \int_{\Sigma}\int \dot{g}(\bar{t})d\xi \approx \Delta\sigma D^3(1/r^{n'})\left[\frac{g(t-r/V) - g(t-r/V-t_r)}{t_r}\right] \quad t_r \sim D/V_r \tag{B4}$$

t_r is the rupture duration, n' includes both the decay due to spreading and attenuation, V_r is the rupture velocity that $\sim V_s$ [*Ben-Menahem and Singh*, 1981], and $\frac{dg}{dt} = \frac{\partial g}{\partial \xi}\left(\frac{\partial \bar{t}}{\partial \xi}\right)^{-1}$. Typically the source time function is ramp-like, so that the expression in square brackets in equation (B4) describes an approximate boxcar function, scaled by t_r and we see that the far-field displacement time domain amplitude scales as D^2. We can approximate the relationship between the peak amplitude in the time domain (B4) and spectral amplitudes, noting that the time domain amplitude of a band-limited wavelet is proportional to the product of its spectral amplitude and twice the bandwidth [*Aki and Richards*, 1980]; thus, assuming the shear wave spectrum is approximately flat to $f\sim^{\pi Vr}/D$ (periods $> > t_r$), we expect a time domain amplitude of D^m corresponds to a spectral amplitude of $D^{(m+1)}$. This predicts the familiar far-field spectral-amplitude scaling of displacement as D^3. More explicitly, if the bracketed expression in (B4) is a boxcar, in the frequency domain this corresponds to a sinc function, with a spectrum that scales as

$$U(\rightharpoonup x,f) \propto (\Delta\sigma/r^n)D^3 \sin c\left[\frac{\pi f D}{V_r}\right] \tag{B5}$$

[*Kanamori and Anderson*, 1975; *Ben-Menahem and Singh*, 1981]. The sinc function effectively reduces the fault dimension in the rupture direction and that for $f < < {}^{\pi Vr}/D$, $\mathrm{sinc}({}^{\pi Vr}/D)\sim1$ and for $f\sim{}^{\pi Vr}/D$ $\mathrm{sinc}({}^{\pi Vr}/D)\sim{}^{V}r/D$. Again, at low frequencies we have the familiar result that the displacement spectrum scales as D^3. The scaling of equation (B5) predicts with an effectively decreasing power of D as frequency increases such that at frequencies at or above $1/t_r$, the far-field displacement scales with D^2. Noting that velocities are high-passed versions of the displacement and accelerations high-passed versions of velocities, we expect that the scaling exponents of D for velocity and acceleration diminish increasingly relative to that for displacement. Albeit a limited data set, our results for the Japanese HiNet observations are consistent with this. Additionally, published values of m for studies of both PGV and PGA always show it to be less for PGA.

[56] The study of *Brune* [1970] also provides insight into the scaling with D. *Brune* [1970] showed that for a tangential stress pulse applied across a fault surface, very close to the fault and before energy arrives from its ends, the shear wave displacement can be described in the time and frequency domains as

$$u(t) = (\Delta\sigma/\mu)V_s t, U(f) = -(\Delta\sigma/\mu)V_s(2\pi f)^2 \tag{B6}$$

respectively [*Brune*, 1970, equations (2) and (3)]. Thus, very close to the fault the displacement depends only on the stress changes immediately nearby and effectively is "blind" to the rest of the fault or, equivalently, is independent of the rupture dimensions. As energy arrives from the rupture boundaries, the velocity becomes a pulse and the displacement can be described in the time and frequency domains as

$$u(t) = (\Delta\sigma/\mu)V_s\tau\left[1 - e_r^{-(t/t)}\right],$$
$$U(f) = -(\Delta\sigma/\mu)V_s(2\pi f)^{-1}\left[(2\pi f)^2 + (V_r/D)^2\right]^{-1/2} \quad \text{(B7)}$$

[*Brune*, 1970, equations (13) and (15)]. At large distances, in the far-field energy diffracts from the opposing sides of the fault, effectively differentiating its signature, and spreading becomes spherical (i.e., scaled by D/r) so that the displacement can be described in the time and frequency domains as

$$u(t) = C(\Delta\sigma/\mu)(D/r)V_s t' e_r^{-(t'/\alpha t)}, t' = (t - r/V_s),$$
$$u(f) = C(\Delta\sigma/\mu)V_s(D/r)\left[(2\pi f)^2 + (2.34V_r/D)^{2)}\right]^{-1} \quad \text{(B8)}$$

C and α are constants required to balance energy [*Brune*, 1970, equations (17) and (20)]. As above, this predicts that the time domain displacement peaks at $t = \alpha D/V_r$ with amplitudes proportional to D^2, and that spectral amplitudes at low frequencies scale as D^3.

Appendix C

[57] We comment briefly on the expected characteristics of dynamic deformations observed at a single location at r and how we measure T and thus $P(r, D)$, assuming the triggering deformation is cumulative. Relative to the peak value alone, the cumulative deformation should decay more slowly but scale with rupture dimension similarly. This is because for most wave trains the peak value occurs at the arrival of the shear or surface wave packet, followed by scattered energy, later phases, and lower group velocity surface waves. Assuming an exponential decrease with time after the peak value, $pk(r, D)$, and neglecting the signal before, we can describe the shape of a wave train as

$$pk(r,D) \times \frac{1}{\gamma(r)}\left[1 - e^{-\gamma(r)T(r)}\right] \sim pk(r,D) \times \frac{1}{\gamma(r)} \qquad T >> 1/\gamma \quad \text{(C1)}$$

Dispersion and scattering effects require that the decay rate, γ, decreases with increasing r, and thus the product of $pk(r, D)$ and $1/\gamma(r)$ must decay more slowly than $pk(r, D)$ alone. Accounting for the signal before the arrival does not change this, because it also lengthens with increasing r.

[58] While the duration of cumulative deformation should account for all the waves arriving at r, in practice we often do not have sufficiently long recordings for the signal to return to the preevent signal level. Fortunately, the calculation of cumulative signal is relatively insensitive to T since for most seismic signals, most of the cumulative deformation arrives in a short interval surrounding the peak value. Thus the measurement duration only needs to be long enough to capture this and the error due to the missing deformation should be independent of r. We achieve this by defining T as the duration required for the signal to diminish to some fraction, ζ, of the peak value. Thus, measurements will likely underestimate the true durations. To assess the size of this error, we consider an exponential signal as in equation (C1) and note the ratio of the approximate to exact estimate of the cumulative deformation is $\sim(1-\zeta)$. Thus, the true probabilities will be underestimated by $100\zeta\%$, so that choice of a small value of ζ results in a small error.

[59] **Acknowledgments.** The authors thank Emily Brodsky for her patient participation in numerous discussions and her many suggestions. They also thank Ken Campbell, David Hill, David Marson, Agnes Helmstetter, Ian Main, and Steven Cohen for their thoughtful comments on the analyses and manuscript.

References

Abrahamson, N. A., and K. M. Shedlock (1997), Overview (Special Issue on Ground Motion Attenuation Relationships), *Seismol. Res. Lett.*, *68*, 9–23.

Aki, K., and P. G. Richards (1980), *Quantitative Seismology, Theory and Methods*, vol. I, pp. 826–827, W.H. Freeman, San Francisco, Calif.

Anderson, J. G. (2000), Expected shape of regressions for ground-motion parameters on rock, *Bull. Seismol. Soc. Am.*, *90*, S43–S52, doi:10.1785/0119960171.

Bak, P., K. Christensen, L. Danon, and T. Scanlon (2002), Unified scaling law for earthquakes, *Phys. Rev. Lett.*, *88()*, 178501, doi:10.1103/PhysRevLett.88.178501.

Beeler, N. M., and D. A. Lockner (2003), Why earthquakes correlate weakly with the solid Earth tides: Effects of periodic stress on the rate and probability of earthquake occurrence, *J. Geophys. Res.*, *108*(B8), 2391, doi:10.1029/2001JB001518.

Ben-Menahem, A., and S. J. Singh (1981), *Seismic Waves and Sources*, pp. 229–242, Springer, New York.

Boatwright, J., H. Bundock, J. Luetgert, L. Seekins, L. Gee, and P. Lombard (2003), The dependence of PGA and PGV on distance and magnitude inferred from northern California ShakeMap data, *Bull. Seismol. Soc. Am.*, *93*, 2043–2055, doi:10.1785/0120020201.

Bragato, P. L. (2005), Estimating an upper limit probability distribution for peak ground acceleration using the randomly clipped normal distribution, *Bull. Seismol. Soc. Am.*, *95*, 2058–2065, doi:10.1785/0120040213.

Bragato, P. L., and D. Slejko (2005), Empirical Ground-Motion Attenuation Relations for the Eastern Alps in the Magnitude Range 2.5–6.3, *Bull. Seismol. Soc. Am.*, *95*, 252–276, doi:10.1785/0120030231.

Brodsky, E. E., and S. G. Prejean (2005), New constraints on mechanisms of remotely triggered seismicity at Long Valley Caldera, *J. Geophys. Res.*, *110*, B04302, doi:10.1029/2004JB003211.

Brune, J. N. (1970), Tectonic stress and the spectra of seismic shear waves from earthquakes, *J. Geophys. Res.*, *75*, 4997–5009.

Brune, J. N. (1976), The physics of earthquake strong motion, in *Seismic Risk and Engineering Decisions*, edited by C. Lomnitz and E. Rosenblueth, pp. 141–177, Elsevier, New York.

Campbell, K. W., and Y. Bozorgnia (2007), Campbell-Bozorgnia NGA empirical ground motion model for the average horizontal component of PGA, PGV and SA at selected spectral periods ranging from 0.01–10.0 seconds, interim report, Pac. Earthquake Eng. Res. Cent., Berkeley, Calif.

Cotton, F., and O. Coutant (1997), Dynamic stress variations due to shear faults in plane-layered medium, *Geophys. J. Int.*, *128*, 676–688, doi:10.1111/j.1365-246X.1997.tb05328.x.

Dieterich, J. A. (1994), Constitutive law for the rate of earthquake production and its application to earthquake clustering, *J. Geophys. Res.*, *99*, 2601–2618, doi:10.1029/93JB02581.

Felzer, K. R. (2005), Evidence that stress amplitude does not affect the temporal distribution of aftershocks, *Eos Trans. AGU*, *86*(52), Fall Meet. Suppl., Abstract S11C-05.

Felzer, K. R., and E. E. Brodsky (2006), Evidence for dynamic aftershock triggering from earthquake densities, *Nature*, *441*, doi:10.1038/nature04799.

Felzer, K. R., and D. Kilb (2006), The June 2005 southern California Anza earthquake: An examination of the extended aftershock zone and intermediate range triggering of the Yucaipa earthquake, *Seismol. Res. Lett.*, *77*, 255.

Felzer, K. R., R. E. Abercrombie, and G. Ekstrom (2004), A common origin for aftershocks, foreshocks, and multiplets, *Bull. Seismol. Soc. Am.*, *94*, 88–98, doi:10.1785/0120030069.

Frankel, A. (2006), Scaling of high-frequency ground motions for the Sumatra, Chi-Chi, and Kocaeli earthquake sequences, *Seismol. Res. Lett.*, *77*, 264.

Freed, A. M. (2005), Earthquake triggering by static, dynamic, and postseismic stress transfer, *Annu. Rev. Earth Planet. Sci.*, *33*, 335–367, doi:10.1146/annurev.earth.33.092203.122505.

Garcia, D., S. K. Singh, M. Herraiz, M. Ordaz, and J. F. Pacheco (2005), Inslab earthquakes of central Mexico: Peak ground motion parameters and response spectra, *Bull. Seismol. Soc. Am.*, *95*, 2272–2282, doi:10.1785/0120050072.

Gomberg, J. (2001), The failure of earthquake failure models, *J. Geophys. Res.*, *106*, 16,253–16,264, doi:10.1029/2000JB000003.

Gomberg, J., and D. C. Agnew (1996), The accuracy of seismic estimates of dynamic strains from Pinyon Flat Observatory, California, strainmeter and seismograph data, *Bull. Seismol. Soc. Am.*, *86*, 212–220.

Gomberg, J., and P. Johnson (2005), Dynamic triggering of earthquakes, *Nature*, *437*, 830, doi:10.1038/437830a.

Gomberg, J., P. Bodin, and P. Reasenberg (2003), Observing earthquakes triggered in the near field by dynamic deformations, *Bull. Seismol. Soc. Am.*, *93*, 118–138, doi:10.1785/0120020075.

Hanks, T., and H. Kanamori (1979), A moment magnitude scale, *J. Geophys. Res.*, *84*, 2348–2350, doi:10.1029/JB084iB05p02348.

Hanks, T. C., and R. K. McGuire (1981), The character of high-frequency strong ground motion, *Bull. Seismol. Soc. Am.*, *71*, 2071–2095.

Helmstetter, A., Y. Y. Kagan, and D. D. Jackson (2005), Importance of small earthquakes for stress transfers and earthquake triggering, *J. Geophys. Res.*, *110*, B05S08, doi:10.1029/2004JB003286.

Helmstetter, A., Y. Y. Kagan, and D. D. Jackson (2006), Comparison of short-term and time-independent earthquake forecast models for southern California, *Bull. Seismol. Soc. Am.*, *96*, 90–106, doi:10.1785/0120050067.

Hertzberg, R. W. (1995), *Deformation and Fracture Mechanics of Engineering Materials*, chap. 12–13, pp. 457–600, John Wiley, New York.

Hill, D. P., and S. G. Prejean (2007), Dynamic triggering, in *Earthquake Seismology Treatise on Geophysics*, *Earthquake Seismol.*, vol. 4, edited by H. Kanamori, chap. 8, pp. 257–291, Elsevier, New York.

Jaeger, J., and N. W. Cook (1979), *Fundamentals of Rock Mechanics*, CRC Press, Boca Raton, Fla.

Johnson, P., and X. Jia (2005), Nonlinear dynamics, granular media and dynamic earthquake triggering, *Nature*, *437*, 871–874, doi:10.1038/nature04015.

Kagan, Y. Y. (1991), Fractal dimension of brittle fracture, *J. Nonlinear Sci.*, *1*, 1–16, doi:10.1007/BF01209146.

Kagan, Y. Y. (2007), Earthquake spatial distribution: The correlation dimension, *Geophys. J. Int.*, *168*(3), 1175–1194, doi:10.1111/j.1365-246X.2006.03251.x.

Kagan, Y. Y., and L. Knopoff (1980), Spatial distribution of earthquakes: The two-point correlation function, *Geophys. J.R. Astron. Soc.*, *62*, 303–320.

Kanamori, H., and D. Anderson (1975), Theoretical basis of some empirical relations in seismology, *Bull. Seismol. Soc. Am.*, *65*, 1073–1095.

Kanno, T., A. Narita, N. Morikawa, H. Fujiwara, and Y. Fukushima (2006), A new attenuation relation for strong ground motion in Japan based on recorded data, *Bull. Seismol. Soc. Am.*, *96*, 879–897, doi:10.1785/0120050138.

Liu, K. S., and Y. B. Tsai (2005), Attenuation relationships of peak ground acceleration and velocity for crustal earthquakes in Taiwan, *Bull. Seismol. Soc. Am.*, *95*, 1045–1058, doi:10.1785/0120040162.

Love, A. (1927), *Mathematical Theory of Elasticity*, Cambridge Univ. Press, New York.

McGarr, A., and J. B. Fletcher (2007), Near-Fault peak ground velocity from earthquake and laboratory data, *Bull. Seismol. Soc. Am.*, *97*, 1502–1510, doi:10.1785/0120060268.

Motazedian, D., and G. M. Atkinson (2005), Stochastic finite-fault modeling based on a dynamic corner frequency, *Bull. Seismol. Soc. Am.*, *95*, 995–1010, doi:10.1785/0120030207.

Pankow, K. L., and J. C. Pechmann (2004), The SEA99 ground-motion predictive relations for extensional tectonic regimes: Revisions and a new peak ground velocity relation, *Bull. Seismol. Soc. Am.*, *94*, 341–348, doi:10.1785/0120030010.

Perfettini, H., and J.-P. Avouac (2004), Postseismic relaxation driven by brittle creep: A possible mechanism to reconcile geodetic measurements and the decay rate of aftershocks, application to the Chi-Chi earthquake, Taiwan, *J. Geophys. Res.*, *109*, B02304, doi:10.1029/2003JB002488.

Perfettini, H., and J.-P. Avouac (2007), Modeling afterslip and aftershocks following the 1992 Landers earthquake, *J. Geophys. Res.*, *112*, B07409, doi:10.1029/2006JB004399.

Pollitz, F., and M. Johnston (2006), Direct test of static versus dynamic stress triggering of aftershocks, *Geophys. Res. Lett.*, *33*, L15318, doi:10.1029/2006GL026764.

Power, M., B. Chiou, N. Abrahamson, Y. Bozorgnia, T. Shantz, and C. Roblee (2008), An overview of the NGA project, *Earthquake Spectra*, *24*(1), 3–21.

Reasenberg, P. A., and L. M. Jones (1989), Earthquake hazard after a mainshock in California, *Science*, *243*, 1173–1176.

Richter, C. F. (1935), An instrumental earthquake-magnitude scale, *Bull. Seismol. Soc. Am.*, *25*, 1–32.

Sabetta, F., and A. Pugliese (1987), Attenuation of peak horizontal acceleration and velocity from Italian strong-motion records, *Bull. Seismol. Soc. Am.*, *77*, 1491–1514.

Savage, H. M., and C. Marone (2008), Potential for earthquake triggering from transient deformations, *J. Geophys. Res.*, *113*, B05302, doi:10.1029/2007JB005277.

Savage, J. C., and S.-B. Yu (2007), Postearthquake relaxation and aftershock accumulation linearly related after the 203 M 6.5 Chengkung, Taiwan, and the 2004 M 6.0 Parkfield, California, earthquakes, *Bull. Seismol. Soc. Am.*, *97*(5), 1632–1645, doi:10.1785/0120070069.

Savage, J. C., J. L. Svarc, and S.-B. Yu (2007a), Postearthquake relaxation and aftershock accumulation linearly related after the 2003 *M* 6.5 Chengkung, Taiwan, and the 2004 *M* 6.0 Parkfield, California, earthquakes, *Bull. Seismol. Soc. Am.*, *97*, 1632–1645, doi:10.1785/0120070069.

Savage, J. C., J. L. Svarc, and S.-B. Yu (2007b), Postseismic relaxation and aftershocks, *J. Geophys. Res.*, *112*, B06406, doi:10.1029/2006JB004584.

Shearer, P., E. Hauksson, and G. Lin (2005), Southern California hypocenter relocation with waveform cross correlation, part 2: Results using source-specific station terms and cluster analysis, *Bull. Seismol. Soc. Am.*, *95*, 904–915, doi:10.1785/0120040168.

Snieder, R., and A. van den Beukel (2004), The liquefaction cycle and the role of drainage in liquefaction, *Granul. Matter*, *6*, 1–9, doi:10.1007/s10035-003-0151-9.

Steacy, S., J. Gomberg, and M. Cocco (2005), Introduction to special section: Stress transfer, earthquake triggering, and time-dependent seismic hazard, *J. Geophys. Res.*, *110*, B05S01, doi:10.1029/2005JB003692.

Wells, D. L., and K. J. Coppersmith (1994), New empirical relationships among magnitude, rupture length, rupture width, rupture area, and surface displacement, *Bull. Seismol. Soc. Am.*, *84*, 974–1002.

Wu, Y., T. Shin, and C. Chang (2001), Near real-time mapping of PGV following a strong earthquake, *Bull. Seismol. Soc. Am.*, *91*, 1218–1228, doi:10.1785/0120000734.

K. Felzer, U. S. Geological Survey, 525 South Wilson Avenue, Pasadena, CA 92206, USA. (kfelzer@usgs.gov)

J. Gomberg, U. S. Geological Survey, Department of Earth and Space Sciences, University of Washington, Box 351310, Seattle, WA 98195-1310, USA. (gomberg@usgs.gov)